AD-A040 946 PENNSYLVANIA STATE UNIV UNIVERSITY PARK APPLIED RESE--ETC F/G 20/1
NOISE DUE TO THE INTERACTION OF BOUNDARY LAYER TURBULENCE WITH --ETC(U)
OCT 76 N MOISEEV, B LAKSHMINARAYANA N00017-73-C-1418
UNCLASSIFIED TM-76-258 NL

1 OF 2
ADA040946

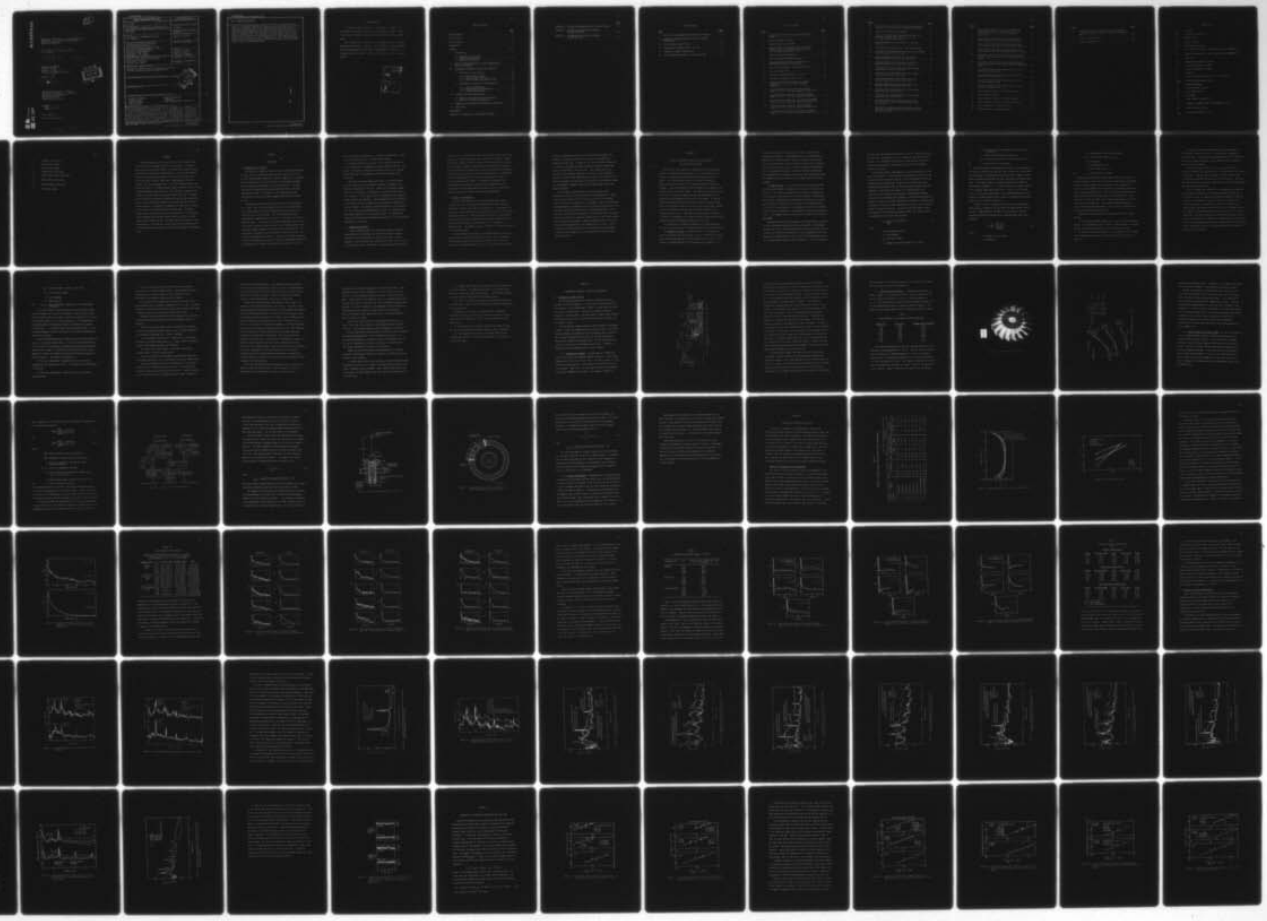

AD A040946

(12)

(6)

NOISE DUE TO THE INTERACTION OF BOUNDARY LAYER TURBULENCE WITH A MARINE PROPULSOR OR AN AIRCRAFT COMPRESSOR.

(10) Neil Moiseev, B. Lakshminarayana and D. E. Thompson

(11) 11 Oct 76

(12) 122 p.

(9) Technical Memorandum
File No. 76-258
October 11, 1976
Contract No. N00017-73-C-1418

(15)

Copy No. 5

(14) TM-76-258

DDC
RECEIVED
JUN 24 1977
C

The Pennsylvania State University
Institute for Science and Engineering
APPLIED RESEARCH LABORATORY
Post Office Box 30
State College, PA 16801

APPROVED FOR PUBLIC RELEASE
DISTRIBUTION UNLIMITED

NAVY DEPARTMENT

NAVAL SEA SYSTEMS COMMAND

AD No. 1
DDC FILE COPY

391 007

REPORT DOCUMENTATION PAGE

READ INSTRUCTIONS BEFORE COMPLETING FORM

1. REPORT NUMBER: TM 76-258
2. GOVT ACCESSION NO.:
3. RECIPIENT'S CATALOG NUMBER:

4. TITLE (and Subtitle): NOISE DUE TO THE INTERACTION OF BOUNDARY LAYER TURBULENCE WITH A MARINE PROPULSOR OR AN AIRCRAFT COMPRESSOR

5. TYPE OF REPORT & PERIOD COVERED: MS Thesis

6. PERFORMING ORG. REPORT NUMBER: TM 76-258

7. AUTHOR(s): Neil Moissev, B. Lakshminarayana and D. E. Thompson

8. CONTRACT OR GRANT NUMBER(s): N00017-73-C-1418

9. PERFORMING ORGANIZATION NAME AND ADDRESS: The Pennsylvania State University, Applied Research Laboratory, P. O. Box 30, State College, PA 16801

10. PROGRAM ELEMENT, PROJECT, TASK AREA & WORK UNIT NUMBERS:

11. CONTROLLING OFFICE NAME AND ADDRESS: Naval Sea Systems Command, Department of the Navy, Washington, D. C. 20362

12. REPORT DATE: October 11, 1976

13. NUMBER OF PAGES: 120 pages & figures

14. MONITORING AGENCY NAME & ADDRESS(if different from Controlling Office): David W. Taylor Naval Ship R&D Center, Department of the Navy, Bethesda, MD 20084

15. SECURITY CLASS. (of this report): Unclassified, Unlimited

15a. DECLASSIFICATION/DOWNGRADING SCHEDULE:

16. DISTRIBUTION STATEMENT (of this Report)

Approved for public release, distribution unlimited, per NSSC (Naval Sea Systems Command), 11/1/76

17. DISTRIBUTION STATEMENT (of the abstract entered in Block 20, if different from Report)

18. SUPPLEMENTARY NOTES

19. KEY WORDS (Continue on reverse side if necessary and identify by block number)

AIRCRAFT COMPRESSOR
BOUNDARY LAYER
MARINE PROPULSOR
RADIATED NOISE
ROTATING BLADE ROW
TURBULENCE
TURBULENCE-PROPULSOR INTERACTION

20. ABSTRACT (Continue on reverse side if necessary and identify by block number)

The sound generated by the interaction of inlet boundary layer turbulence with a rotating blade row is investigated. To experimentally study this radiated sound, an existing aeroacoustic facility was modified to produce the inflows desired. The rotor was operated in air with different blade space-to-chord ratios, different flow coefficients and different anisotropic, nonhomogeneous turbulent inflows. The inflows ingested are: (1) natural boundary layer on hub and annulus wall, (2) a tripped boundary layer on the hub, and (3) a fully developed boundary layer on the hub. The turbulence intensities and length

→ next page

20. ABSTRACT (Continued)

scales were altered by placing a grid at the inlet. The mean velocity profiles, turbulence intensities, length scales, and energy spectra of the inflow were measured, as well as near and far-field acoustic spectra. A parametric investigation of the effect of inflow characteristics on the radiated sound has been made. The sound pressure level is found to be directly proportional to the turbulence intensity squared and inversely proportional to the ratio of axial length scale to blade spacing. Two length scales were found to exist simultaneously. The long axial length scales are the dominant factor in tone noise production, while the short scales dominate the broadband noise.

ACKNOWLEDGMENTS

The authors wish to thank Dr. J. Clay and Mr. J. Rishell for their help in carrying out the hot wire measurements and Mr. W. Nuss for his help in the data reduction and making the acoustical measurements.

This research was carried out at the Applied Research Laboratory, The Pennsylvania State University, under the Naval Sea Systems Command General Hydromechanics Research Program Subproject SR 023 01 01, administered by the David W. Taylor Naval Ship Research and Development Center.

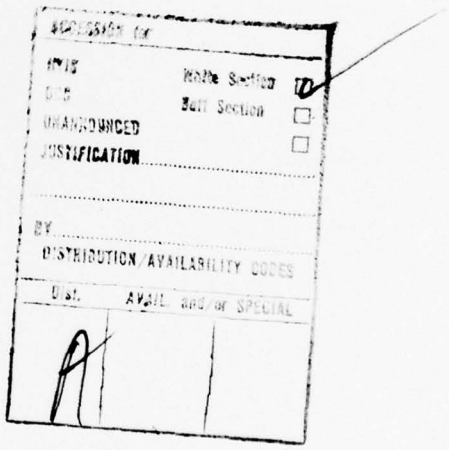

TABLE OF CONTENTS

	Page
ACKNOWLEDGMENTS	ii
LIST OF TABLES	v
LIST OF FIGURES	vi
NOMENCLATURE	x
ABSTRACT	xiv
I. INTRODUCTION	1
1.1 Statement of the Problem	1
1.2 Engineering Importance	2
1.3 Method of Investigation	3
II. REVIEW OF TURBULENCE SOURCES, NOISE MECHANISMS AND PRIOR INVESTIGATIONS	5
III. EXPERIMENTAL EQUIPMENT, METHODS AND TECHNIQUES	18
3.1 Description of Test Facility	18
3.1.1 Semi-Anechoic Chamber	18
3.1.2 Test Rotor and Inlet Duct	21
3.1.3 Baffle Chamber and Screen Diffuser	24
3.2 Experimental Procedure and Instrumentation	25
3.2.1 Inlet Configurations	25
3.2.2 Aerodynamic Flow Measurements	25
3.2.3 Acoustic Measurements	32
IV. DISCUSSION OF EXPERIMENTAL RESULTS	34
4.1 Results of Aerodynamic Flow Measurements	34
4.2 Results of Acoustic Measurements	52
V. CORRELATION OF TURBULENCE PARAMETERS WITH NOISE DATA	73
VI. CONCLUSIONS	85
BIBLIOGRAPHY	87
APPENDIX A: CALIBRATION OF SEMI-ANECHOIC CHAMBER	90

Page

APPENDIX B: STEADY STATE CHARACTERISTICS OF THE TEST ROTOR 92

APPENDIX C: ATTEMPTS TO ACHIEVE FULLY DEVELOPED BOUNDARY LAYER FLOW 100

APPENDIX D: CALIBRATION OF THE ACOUSTIC RESPONSE OF THE INLET DUCT 104

LIST OF TABLES

Table		Page
I	Rotor Chord and Stagger Angle Variation with Radius	21
II	Summary of Boundary Layers and Far-Field Acoustic Measurements	35
III	Axial Integral Length Scales	42
IV	Average Axial Integral Scales - No Grid	47
V	Tangential Integral Length Scales	51
VI	Rotor Operating Conditions - Steady State Test	92

LIST OF FIGURES

Figure		Page
1	Turbomachinery Noise Facility and Semi-Anechoic Chamber	19
2	Seventeen Bladed Test Rotor	22
3	Blade Profiles at Three Radii	23
4	Boundary Layer Duct Configurations: (a) Natural Boundary Layer, (b) Artificial Boundary Layer, (c) Fully Developed Boundary Layer	26
5	Diagram of Flow Instrumentation	28
6	Plan View Showing Measuring Stations	30
7	Diagram Showing Two Probe Configuration for Determining Tangential Length Scales	31
8	Mean Velocity Profiles - With and Without Grid	36
9	Law of the Wall Plots	37
10	Turbulence Intensity Profiles - No Grid	39
11	Turbulence Intensity Profiles - Grid	40
12	Typical Auto-Correlation Curves for Natural Boundary at ϕ = 0.75, 5440 rpm, Seventeen Bladed Rotor	41
13	Auto-Correlation Curves for Natural Boundary Layer at ϕ = 0.75, 5440 rpm, Seventeen Bladed Rotor	43
14	Auto-Correlation Curves for Artificial Boundary Layer at ϕ = 0.75, 5440 rpm, Seventeen Bladed Rotor	44
15	Auto-Correlation Curves for Fully Developed Boundary Layer at ϕ = 0.75, 5440 rpm, Seventeen Bladed Rotor	45
16	Cross-Correlation Curves for Natural Boundary Layer at ϕ = 0.75, 5440 rpm, Seventeen Bladed Rotor	48
17	Cross-Correlation Curves for Artificial Boundary Layer at ϕ = 0.75, 5440 rpm, Seventeen Bladed Rotor	49

Figure		Page
18	Cross-Correlation Curves for Fully Developed Boundary Layer at ϕ = 0.75, 5440 rpm, Seventeen Bladed Rotor . . .	50
19	Normalized Turbulent Energy Spectra	53
20	Typical Rotor Noise and Background Levels for Fully Developed Boundary Layer with Grid, ϕ = 0.75, 5440 rpm, Seventeen Bladed Rotor	54
21	Seventeen-Bladed Rotor Sound Spectra - Near and Far Field	55
22	Ten-Bladed Rotor Sound Spectra - Near and Far Field . . .	56
23	Comparison of Nondimensional Seventeen- and Ten-Bladed Rotor Sound Spectra for Far Field	58
24	Seventeen-Bladed Rotor Sound Spectra for Three Boundary Layers with No Grid for Near Field	59
25	Seventeen-Bladed Rotor Sound Spectra for Three Boundary Layers with No Grid for Far Field	60
26	Ten-Bladed Rotor Sound Spectra for Three Boundary Layers with No Grid for Near Field	61
27	Ten-Bladed Rotor Sound Spectra for Three Boundary Layers with No Grid for Far Field	62
28	Seventeen-Bladed Rotor Sound Spectra for Three Boundary Layers with Grid for Near Field	63
29	Seventeen-Bladed Rotor Sound Spectra for Three Boundary Layers with Grid for Far Field	64
30	Ten-Bladed Rotor Sound Spectra for Three Boundary Layers with Grid for Near Field	65
31	Ten-Bladed Rotor Sound Spectra for Three Boundary Layers with Grid for Far Field	66
32	Seventeen-Bladed Rotor Sound Spectra for Three Flow Coefficients for the Natural Boundary Layer with No Grid	69
33	Comparison of Seventeen- and Ten-Bladed Rotor Sound Spectra for Natural Boundary Layer with No Grid for Far Field, 0-10 kHz	70

Figure		Page
34	Blade Passing Frequency Tone Time Histories for Natural and Artificial Boundary Layers With and Without Grid, ϕ = 0.75, 5440 rpm, Seventeen Bladed Rotor	72
35	Correlation Between Blade Passing Frequency Tone Sound Pressure Level and Tip Turbulence Values	74
36	Correlation Between Blade Passing Frequency Tone Sound Pressure Level and Root Turbulence Parameters	75
37	Correlation Between Blade Passing Frequency Tone Sound Pressure Level and Mid-Radius Turbulence Values	77
38	Correlation Between Blade Passing Frequency Second Harmonic Tone Sound Pressure Level and Tip Turbulence Values	78
39	Correlation Between Second Blade Passing Frequency Harmonic Tone Sound Pressure Level and Root Turbulence Values	79
40	Correlation Between Sound Pressure Level at 2 kHz and Tip Turbulence Values	80
41	Correlation Between Sound Pressure Level at 2 kHz and Root Turbulence Values	81
42	Correlation Between Sound Pressure Level at 4 kHz and Tip Turbulence Values	83
43	Correlation Between Sound Pressure Level at 4 kHz and Root Turbulence Values	84
44	Inverse Square Law Test for Semi-Anechoic Room	91
45	Exit Velocity Profiles	94
46	Stage Loading Coefficient vs. Radial Position	95
47	Static Pressure Coefficient vs. Radial Position	96
48	Lift Coefficient vs. Radial Position	98
49	Drag Coefficient vs. Radial Position	99

Figure		Page
50	Cross-Section View of Boundary Layer Configurations: (a) O-Ring Transition Trip, (b) Screws, (c) Sandpaper Alone	101
51	Inlet Velocity Profiles	102
52	Acoustic Response of Duct	106

NOMENCLATURE

A	a constant
ABL	artificial boundary layer
a_0	speed of sound
B	number of blades
BPF	blade passing frequency
C_L	lift coefficient based on cascade mean velocity (Appendix B)
C_D	drag coefficient based on cascade mean velocity (Appendix B)
c	blade chord
E + e	instantaneous anemometer voltage
E	DC part of anemometer voltage
e	AC part of anemometer voltage
f	frequency
F	slope of King's law equation $(E + e)^2 = E_0^2 + F\sqrt{V}$
FDBL	fully developed boundary layer
g(f)	frequency parameter
I	sound intensity in watts
IGV	inlet guide vane(s)
k	wave number
L_x	axial integral length scale
L_θ	tangential integral length scale [Equation (3.4)]
M_a	axial Mach number, U_x/a_0
M_{rel}	relative Mach number, U_{rel}/a_0

M_T	tip Mach number, U_T/a_0
NBL	natural boundary layer
P_m	measured static pressure
P_0	stagnation pressure
P_s	static pressure
q, $\sqrt{\overline{q^2}}$	turbulent velocity component normal to blade surface
r	radius
r_h	hub radius
r_T	tip radius
S	blade spacing, $2\pi r/B$
SPL	sound pressure level
T	integral time scale [Equation (3.3)]
t	time
u, $\sqrt{\overline{u^2}}$	axial turbulent velocity fluctuations
u'	axial turbulence intensity, $\sqrt{\overline{u^2}}/U_c$
U_c	center mean axial velocity (absolute)
U_{rel}	flow velocity relative to blade, $\sqrt{U_x^2 + (\Omega r)^2}$
U_T	blade tip speed
U_x	local axial mean velocity (absolute)
U_θ	local tangential mean velocity (absolute)
$\sqrt{\overline{v^2}}$	tangential turbulent velocity fluctuations

v'	tangential turbulence intensity, $\sqrt{\overline{v^2}}/U_c$
V	velocity component normal to hot wire sensor
W	total sound power
W_m	mean relative flow velocity
x	axial position
y	distance
α	absolute flow angle
β_1	inlet flow angle
β_1'	inlet blade angle
β_2	exit flow angle
β_2'	exit blade angle
β_m	mean flow angle
Γ	nondimensional frequency $(2\pi f L_x/U_x)$
γ	angle of hot wire sensor in relation to center line
ζ	stagger angle
θ	angle of probe separation in circumferential direction
λ	wavelength
ϕ	flow coefficient, (U_c/U_T)
π	3.14 ...
ρ	fluid density
$\rho_{uu}(\tau)$	auto-correlation coefficient [Equation (3.3)]
$\rho_{vv}(\theta)$	cross-correlation coefficient [Equation (3.4)]

σ	solidity of rotor, c/S
τ	delay time, seconds
χ	acoustic wave number
ψ	average lift curve slope
ψ_E	ideal pressure rise coefficient
ψ_0	stage loading coefficient
ψ_s	static pressure coefficient
Ω	rotor shaft speed

ABSTRACT

The sound generated by the interaction of inlet boundary layer turbulence with a rotating blade row is investigated. To experimentally study this radiated sound, an existing aeroacoustic facility was modified to produce the inflows desired. The rotor was operated in air with different blade space-to-chord ratios, different flow coefficients and different anisotropic, nonhomogeneous turbulent inflows. The inflows ingested are: 1) natural boundary layer on hub and annulus wall, 2) a tripped boundary layer on the hub, and 3) a fully developed boundary layer on the hub. The turbulence intensities and length scales were altered by placing a grid at the inlet. The mean velocity profiles, turbulence intensities, length scales, and energy spectra of the inflow were measured, as well as near- and far-field acoustic spectra. A parametric investigation of the effect of inflow characteristics on the radiated sound has been made. The sound pressure level is found to be directly proportional to the turbulence intensity squared and inversely proportional to the ratio of axial length scale-to-blade spacing. Two length scales were found to exist simultaneously. The long axial length scales are the dominant factor in tone noise production while the short scales dominate the broadband noise.

CHAPTER I

INTRODUCTION

1.1 Statement of the Problem

Turbulence is an important source of noise generating mechanisms in marine vehicles (propulsors and ventilation fans) as well as in aircraft turbomachinery (propellers, fans and compressors). Propulsor noise is characterized by discrete peaks at blade passing frequency and its harmonics superimposed on a broadband spectrum. The same characteristic radiated sound spectrum has been found for aircraft compressors and fans. The presence of the broadband noise and fluctuations in the discrete peaks suggest generation by a random process.

Investigators have found four major sources for this broadband rotor noise. They are blade boundary layers, vortex shedding from the trailing edge of the blade, separated flows (as in stall), and turbulence in the incoming flow. For low speed propulsors and compressors as considered here, turbulence in the inflow is the most important source. The sources of turbulence upstream of the rotor are: free stream or ambient, annulus and hub or hull boundary layers, and inlet guide vanes (aircraft) or control surface wakes (marine). The interaction of turbulence with the potential flow field of the rotor results in quadrupole noise sources. The noise from marine propulsors or aircraft compressors can also be related to time-dependent pressures on the blades due to random fluctuations in the angle of attack of

the blades caused by operating in a turbulent velocity field. These fluctuating pressures result in dipole noise sources.

Extensive studies have been made of the radiated sound due to a rotor operating in a homogeneous, isotropic turbulent inflow. The present investigation considers the radiated sound due to rotating blades operating in nonhomogeneous, anisotropic boundary layer turbulence.

There are several parameters which affect the radiated sound the most important is the turbulence intensity, a measure of the velocity fluctuations in the flow. Another is the integral length scale of the turbulence, an indication of the typical eddy size of the turbulence. In this study, both the longitudinal and tangential integral scales are considered. These parameters give an indication of the spatial extent and amplitude of the pressure fluctuations on the rotor blades. The measured turbulence parameters are correlated with the radiated sound measurements in an effort to understand the mechanisms responsible for this radiated sound. The experimental results should also provide important ground work for future theoretical development in this field.

1.2 Engineering Importance

A basic understanding of the sources generating the sound in propulsors and turbomachinery will lead to the design of quieter propulsors and power machinery for aircraft and marine vehicles. Research to date has shown that turbulence is a major cause of broad-band noise from rotors. Elimination of turbulence producing devices

upstream (e.g., grilles) would reduce the broadband noise. Since other methods for reducing turbulence can be impractical in terms of engine performance, weight or cost, the operating characteristics of the rotor may be changed to optimize both acoustic and aerodynamic performance. One such change is an optimum rotor solidity resulting from an analysis on the effect of the ratio of turbulence length scales to blade spacing. The rotor blade speed can be lowered, thus reducing the impact of turbulent eddies on the blades. A fundamental knowledge of the relationship between inflow turbulence and noise generated by its interaction with rotating blades would lead not only to better noise prediction but also to better noise reduction techniques.

1.3 Method of Investigation

There are many theories for turbulence-induced noise from a rotating blade row. Most begin by assuming a turbulence model and attempting to predict the noise for an actual fan. Few attempts have been made to relate the actual inlet turbulence to a rotor to the noise produced by that rotor. This is the major objective of this research. In this study, the inlet boundary layer turbulence is measured as well as the noise generated by its interaction with a compressor or propulsor rotor. An attempt is made to relate the turbulence parameters to the radiated sound.

An aeroacoustic test facility at the Applied Research Laboratory was modified to create the necessary inflows for this investigation. Three boundary layers were studied, the boundary layer occurring naturally in the modified test facility, an artificial boundary layer

formed by tripping the inflow, and a fully developed boundary layer produced by covering the hub of the facility with sandpaper and removing the nose cone. In addition, the inlet turbulence properties of intensity and length scale were altered by placing a square mesh grid at the entrance to the inlet duct. The relevant inlet flow parameters were measured utilizing two x-array hot wire anemometer systems. Spectral sound measurements were made for two rotors of the same blade geometry but different blade spacing by recording the output of a microphone on magnetic tape and filtering through a real time spectrum analyzer.

Until recently, there have been no data available on the quantitative effects of inlet turbulence on sound generation. Indeed, little is still known about the actual structure of inlet boundary layer turbulence for a propulsor or a compressor. None of the previous investigations have considered the inflow turbulence properties and the radiated sound for an identical set of operating parameters. One of the major objectives of this research is to gain some basic information about inlet turbulence, especially length scales, in the thick boundary layer as normally encountered in marine propulsors, and the near and far sound fields generated by its interaction with a rotor. Only by relating the turbulence properties to the particular noise spectrum it produces is it possible to fully understand the mechanisms that generate the noise.

CHAPTER II

REVIEW OF TURBULENCE SOURCES, NOISE MECHANISMS AND PRIOR INVESTIGATIONS

The inflow to any propulsor or compressor will have turbulence present. Turbulence is nonuniformity in the flow characterized by velocity fluctuations and small perturbations varying in size, or eddies. In a test stand under static conditions, substantial acceleration occurs near the inlet causing turbulence intensity to increase. From an environmental noise standpoint, the landing of jet powered aircraft is a major example. The engines very often will get a cross flow at the inlet, causing boundary layer separation on the annulus wall which generates high levels of turbulence. For marine propulsors operating in the hull boundary layers or control surface wakes, the turbulence levels at the inlet could be very high. Another source of turbulence is the one that is present naturally in the atmosphere and the ocean. These eddies are distributed at random so a propulsor or compressor will encounter eddies of many different sizes leading to spatial and temporal variations in the flow.

Two mechanisms are considered responsible for noise generation from inlet turbulence, both in an upstream wake and in the free stream:

(A) Quadrupole Sources. Turbulence provides the mechanism by which the potential flow field around the rotor is scattered as sound. Ffowcs-Williams and Hawkings [1] first pointed out this effect. They studied the inhomogeneities of the homogeneous wave equation for a

finite velocity field in the vicinity of a fan. This induces a quadrupole distribution. Chandrashekara [2] later investigated the significance of these sources in detail by measuring the turbulent velocity fluctuations in the axial direction and the axial potential flow field near two test rotors. Then he estimated the sound power due to the quadrupole sources. Both Ffowcs-Williams and Hawkings' and Chandrashekara's investigations indicated that quadrupole sources are insignificant noise generators for low speed fans at low blade loadings.

(B) Dipole Sources. The fluctuating velocity field associated with turbulence produces fluctuations in the angle of attack of the blade row. This leads to unsteady blade forces and the generation of noise due to dipole sources on the blade surfaces. Sevik [3] and Mani [4] both, independently, investigated this theoretically, using Sears' [5] gust function for the calculation of the unsteady blade forces due to inlet turbulence. An extensive review of the literature on the effects of turbulence on noise generation is given in References 6 and 7. An expanded version of this review is given in the following paragraphs.

Qualitative evidence on the dependence of radiated sound intensity on inlet turbulence comes from Sofrin and McCann [8]. They examined the noise due to the viscous interaction of inlet guide vanes, IGV, and a rotor as a function of the distance of the IGV upstream of the rotor. The noise level was observed to fall off with increasing separation up to a certain distance where the noise leveled off. A further decrease

in noise level was detected upon removal of the IGV. Sofrin and McCann concluded that the presence of the IGV raised the turbulence level in the duct. The lowering of the noise level observed when the IGV was removed was attributed to the lowering of the level of turbulence incident on the rotor.

Sharland [9] studied, experimentally, the noise produced by a flat plate in an open jet. With the plate in the potential core of the jet, he found that the noise level was due to lift fluctuations from vortex shedding at the trailing edge. However, when the plate was in the turbulent mixing region of the jet and the turbulent length scale was comparable to the plate chord length, the noise produced by the turbulent velocity fluctuations dominated. Sharland also observed that noise due to boundary layer pressure fluctuations was insignificant compared to noise due to vortex shedding and turbulence. Sharland tried to estimate the level of noise radiated due to airfoil lift fluctuations caused by incident turbulence. He used Curle's [10] acoustic theory and Liepmann's [11] statistical unsteady airfoil lift ideas to derive an expression for the total acoustic power:

$$W = \frac{\rho}{48\pi a_0^3} \int \psi^2 c U_{rel}^4 \overline{(q)^2}\, dy \quad , \tag{2.1}$$

where

W = total acoustic power,

ρ = fluid density,

a_0 = velocity of sound,

ψ = average lift slope defined by $C_L = \psi q / U_T$,

q = turbulent velocity component (RMS value) normal to the chord,

c = blade chord at spanwise location y,

U_{rel} = relative mean velocity of the blade section at y

and U_T = tip velocity of rotor blade.

Morfey [12] studied the broadband noise due to the interaction of the turbulent wakes from an upstream blade row with one or more blade rows downstream. The measured noise resulting from a number of multi-stage compressors was analyzed and some interesting correlations were found. The frequency spectra collapsed reasonably well using the nondimensional parameter ℓ/λ (ℓ is the characteristic length related to the upstream blade drag coefficient, $\ell = 2bC_D$, 2b is the blade chord, λ is the sound wave length). This was surprising because the frequency collapse would have been expected to depend on the Strouhal number, $f\ell/U$ (U is the flow velocity).

A result of the ℓ/λ frequency scaling is that the sound power varies as M_{rel}^5, instead of the M_{rel}^6 predicted using Strouhal number scaling. A semi-empirical collapse of the sound power data was analyzed by Morfey [12] resulting in a nondimensional sound power parameter:

$$G = \frac{dW}{df} \cdot \frac{f^3 S^2 \csc^4 \beta_2}{\rho a_0^5 S_R M_{rel}^5} \quad , \tag{2.2}$$

where

B = number of rotor blades,

f = frequency,

G = nondimensional sound power parameter,

M_{rel} = relative Mach number, U_{rel}/a_0,

s = blade span,

S = blade spacing, $2\pi r/B$,

S_r = rotor blade area $s \cdot c \cdot B$

and β_2 = exit relative flow angle.

Mugridge and Morfey [13] reviewed experimental and theoretical results relating to noise sources. Describing the physical mechanisms by which turbulence generates fluctuations in blade loading, they explain that the broadband noise from subsonic compressors and fans is due to these fluctuating forces. The fluctuations are generated by the random interaction of blade surfaces with the turbulent flow. The turbulence can have its origin in the blade boundary layer or it can be convected with the mean flow. Early experiments [9] showed quite clearly that the mechanisms related to inlet turbulence dominate other sources in many practical applications.

Mugridge and Morfey concluded the following from their investigations:

(1) Fan noise at subsonic speeds may be due to dipole or quadrupole sources. The predominant source of noise in lightly loaded or low speed fans is the dipole type, arising from fluctuating blade forces.

(2) Noise from incident turbulence can be estimated from the blade surface pressure spectrum and the turbulent velocities entering the blade row.

(3) Secondary flows associated with blade tip clearances and duct boundary layers are a source of turbulence and consequently broadband noise. Because they have opposing effects on the secondary flow, tip clearance and boundary layer thickness can be balanced to reduce the noise radiation.

Sevik [3] and Mani [4] were the first to provide an exact analytical procedure for the prediction of radiated noise from a fan due to turbulence. They started by assuming a turbulence model, then calculating the unsteady lift generated by the turbulence. The final step was to predict the acoustic radiation due to the force distribution generated by the unsteady flow.

Sevik [3] assumed the turbulence to be homogeneous and isotropic. He calculated the unsteady lift by using the Sears' [5] function. Sevik predicts that the radiated sound spectrum depends on turbulence intensity, a characteristic time scale based on the ratio of the integral length scale of turbulence to axial flow velocity, and characteristic length scales such as the ratio of the integral scale of turbulence to acoustic wavelength, the radius of the rotor, and the blade chord. The theory does not include any blade-to-blade correlations of the unsteady lift; therefore, the resulting spectrum does not exhibit the characteristic peak at blade passing frequency and harmonics. Sevik's derivation yields the following expression for the spectral density of the sound power:

$$\frac{dW}{d\Gamma} = \pi^3 \left(\frac{\overline{u^2}}{U_x^2}\right) M_a^3 \left(\frac{\rho U_x^3 r_T^2}{1+\phi^2}\right) \left(\frac{r_T}{L_x}\right)^2 \left|1 - \left(\frac{r_h}{r_T}\right)^2\right|^2 \cdot$$

$$g(\Gamma) F_1 \left(\frac{r_T}{L_x}, kr_T\right) \quad , \qquad (2.3)$$

where

$\Gamma = \frac{2\pi f L_x}{U_x}$, nondimensional frequency,

W = sound power in watts,

$\overline{u^2}$ = square of axial turbulent velocity fluctuations, $\sqrt{\overline{u^2}}$,

a_0 = speed of sound,

ρ = fluid density,

U_x = axial flow velocity,

r_T = tip radius of the rotor,

L_x = turbulent axial integral length scale,

$g(\Gamma)$ = frequency parameter defined in Reference 3,

$F_1(r_T/L_x, kr_T)$ = radiation function given in Reference 3,

M_a = axial Mach number, U_x/a_0,

ϕ = flow coefficient,

r_h/r_T = hub-to-tip ratio

and f = frequency (Hz).

Mani's [4] model assumed the turbulence to be homogeneous, isotropic, and weakly stationary with a longitudinal velocity correlation of the type $\exp[-r/L_x]$, r is the separation between points in the

turbulence field and L_x is the length scale of turbulence. Mani used the Sears [5] function to calculate the unsteady lift. Mani's final expression for the radiated sound is:

$$\chi \frac{dI}{d\chi} = \frac{3}{2} \rho U_x \overline{u^2} \cdot \frac{\pi^2 \sigma^2 \chi S}{24 L_x \cos^2\zeta} \cdot \left[\frac{(1-M_a^2)^{1/2}}{2\pi c \chi \sin\zeta} \cdot \log\left\{ \frac{1+2\pi\omega_{r+}}{1+2\pi\omega_{r-}} \right\} \right] \cdot$$

$$\left\{ \int \frac{(1+3\cos^2\zeta)k_x^2 + L_x^{-2} + 6k_x k_y \cos\zeta\sin\zeta + (1+3\sin^2\zeta)k_y^2}{(L_x^{-2} + k_x^2 + k_y^2)^{1/2}} \, dk_y \right\} \cdot$$

$$\sin^2\zeta \left\{ \frac{\pi}{2} + \frac{(1-M_a^2)(\cot^2\zeta - 1)}{2} \cdot \left(- \frac{\pi}{2M_a^2} + \frac{\pi}{2M_a^2(1-M_a^2)^{1/2}} - \right. \right.$$

$$\left. \left. \frac{\arcsin M_a}{M_a^2(1-M_a^2)^{1/2}} + \frac{1}{M_a} \right) \right\} \quad , \tag{2.4}$$

where

I = intensity,

$\overline{u^2}$ = square of axial turbulent velocity fluctuations, $\sqrt{\overline{u^2}}$,

χ = acoustic wavenumber,

ζ = stagger angle of cascade,

L_x = longitudinal integral length scale of turbulence,

M_a = axial Mach number,

σ = blade row solidity, c/S,

c = blade chord,

$\omega_{r\pm} = (c\chi/2M_{rel}\sqrt{1-M_a^2}) \cdot \{\sqrt{1-M_a^2} \pm M_T\}$,

M_{rel} = flow Mach number relative to the rotor,

M_T = rotor tip Mach number,

$k = \chi S$, wavenumber,

S = blade spacing,

and k_x, k_y = axial, tangential component of the nondimensional wavenumber.

It is evident from the above expression that the acoustic energy per unit frequency is a function of frequency, axial flow Mach number, blade tip speed, blade row solidity, turbulence intensity, and the ratio of turbulence length scale to blade spacing, L_x/S. The spectrum has broadband peaks at blade passing frequency and harmonics as long as L_x/S exceeds 0.5. For larger values, the peaks become sharper. While the peaks disappear as L_x/S becomes smaller, the general nondimensional sound levels increase.

Robbins and Lakshminarayana [7] modified Mani's [4] and Sevik's [3] theory to include the cascade effect. To verify this modified theory, they carried out an experimental investigation using a marine propulsor, operated over a range of tip speeds with different turbulence levels generated by grids, and compared the measured radiated sound spectra to predicted spectra. Their major conclusions are:

(i) The total sound power is dependent not only on turbulent intensity but the length scale as well. The sound power is proportional to $\overline{u^2}U_{rel}^4/L_x^2$.

(ii) The sound spectrum had a shape similar to the turbulent energy spectrum.

(iii) The sound spectrum levels produced can be accurately predicted over a limited frequency range. The Sevik-Sears theory's overestimation of noise intensity at lower frequencies can be attributed to interference effects due to a cascade.

(iv) The use of the cascade gust function did not affect the sound pressure level at moderate frequencies (0.7 to 2 kHz). At higher frequencies, the predictions with the cascade gust function were closer to measured sound levels, particularly with Mani's theory.

Thompson [14] has extended Sevik's [3] analysis to include blade-to-blade correlations and predicted the time dependent thrust of a propeller.

Pickett [15] extended Mani's theory to anisotropic turbulence. He used an aerodynamic response function valid for three-dimensional flow developed by Mugridge [16]. Pickett concluded:

(i) The frequency distribution of radiated sound is primarily dependent on the axial length scale, L_x. Large L_x leads to discrete tones at blade passing frequency and harmonics.

(ii) Tonal power levels depend on turbulent intensity and circumferential and radial length scales.

(iii) The division of sound radiation upstream and downstream is strongly dependent on the circumferential and radial length scales.

Lowson [17] assumes that the time dependent lift on a typical blade is known, eliminating the need to model the turbulence and finding an appropriate aerodynamic force function. Lowson's analysis is for a single blade with a weighting function used to expand the

analysis to the multibladed case. The weighting function includes a delta function at blade passing frequency, BPF, and a background level due to random blade-to-blade variations which reach a peak at BPF and harmonics if they are correlated. Lowson concluded that strenuous efforts to reduce nonuniformity in the flow are justified.

Hanson [18] also assumes the time-dependent lift is known. He makes use of random pulse modulation, rpm, theory. The idea for this model was guided by his experimental data on blade pressure distribution and inlet turbulence structure. He found that inlet turbulent eddies are elongated as they are sucked into a static fan and chopped by each blade at least once per revolution of the fan. This gives rise to a train of lift pulses at the rotational frequency. The pulse amplitudes grow and decay according to a pulse envelope function. Eddy irregularities are taken into account through the variable pulse amplitude modulation and pulse position modulation. The latter accounts for changes in the pulse rate. Sound intensity is expressed in terms of an unknown standard pulse function and a joint distribution function derived for the turbulent eddies. These functions have to be determined from direct measurement of the instantaneous lift on the blade. Although Hanson shows good agreement between theory and experiment, a major drawback of his theory is the difficulty of measuring the blade loading in many installations.

Homicz and George [19] developed expressions and conclusions very similar to Mani [4] and Sevik [3]. They also studied the effect of compressibility and distributed loading on the noise from the

interaction of isotropic, homogeneous turbulence with a rotor. They proposed the most critical parameter to be $U_x/L\Omega$, where U_x is axial velocity, L is the turbulent integral scale and Ω is the rotor shaft speed. Large values of this parameter lead to a broadband noise, while progressively smaller values give rise to an increasingly discrete noise spectrum. The chief influence of the compressibility and distributed loading effects is a lowering of high frequency noise radiation. Homicz and George's theory agrees fairly well with the experimental data of Lowson et al. [20].

Lowson et al. [20] conducted an investigation into rotor tip noise. They found it is confined to high frequencies and is easily controlled. They proposed several source mechanisms for tip noise..

Lane [21] performs an analysis using the Green's function relating the radiated pressure field to the fluctuating blade forces. By incorporating dissipation, resonances which would ordinarily occur at the cut-off frequencies of the duct are removed. Lane developed a wave number dependence for effective eddy viscosity.

Cumpsty and Lowrie [22] made noise measurements for in-flight and static conditions and compared the results for different rotor tip numbers. They concluded:

(i) Under typical static test conditions, there are enough unsteady distortions in the inflow to dominate the blade passing frequency, BPF, sound at subsonic rotor tip speeds. These unsteady distortions cause the variation of sound pressure level with time usually associated with rotor BPF tones.

(ii) Boundary layer intake is the dominant source of distortion at low Mach numbers. The momentum thickness of the boundary layer appears to be the best correlating parameter. At higher Mach numbers, low order turbulent eddies become the dominant source.

(iii) There is a significant change in noise between static and in-flight tests. Greater care must therefore be taken in interpreting static noise tests.

Goldstein et al. [23] in a theoretical study included the compressibility effect, convection of eddies by the mean flow, and anisotropic inlet turbulence. The two major conclusions of their analysis are:

(i) When turbulence correlation lengths become equal to blade spacing, the predicted spectra exhibit peaks at tonal frequencies.

(ii) The quadrupole noise source contributes mainly to the broadband spectrum until the correlation lengths of the turbulence become quite large.

CHAPTER III

EXPERIMENTAL EQUIPMENT, METHODS AND TECHNIQUES

3.1 Description of Test Facility

An existing aeroacoustic test facility was modified for the purposes of this investigation. It is the same as Robbins [24] with the exception of a new semi-anechoic chamber, an additional ten bladed rotor, and a modified inlet. The facility, as shown in Figure 1, consists of four main parts: the semi-anechoic chamber which surrounds the inlet, the test rotor, a screen diffuser and baffle chamber, and a Joy axial flow fan.

The semi-anechoic chamber provides a known acoustical environment in which to study the radiated sound from the test rotor. The screen diffuser prevents flow separation and its attendant noise, while the baffle chamber inhibits sound from the Joy fan from reaching the semi-anechoic chamber by an upstream path. The Joy fan permits the control of the rate of flow through the test rotor. A detailed discussion of the aeroacoustic test facility follows:

3.1.1 Semi-Anechoic Chamber. The semi-anechoic chamber was built by the staff at the Applied Research Laboratory. It has inside dimensions of 3.35 m by 3.66 m by 2.44 m. The walls consist of a wood frame with plywood shelves. These shelves are filled with 15.24 cm of fiberglass. There is a 2.54 cm air space between the fiberglass and an outer sheathing of tar paper. The chamber is mounted on

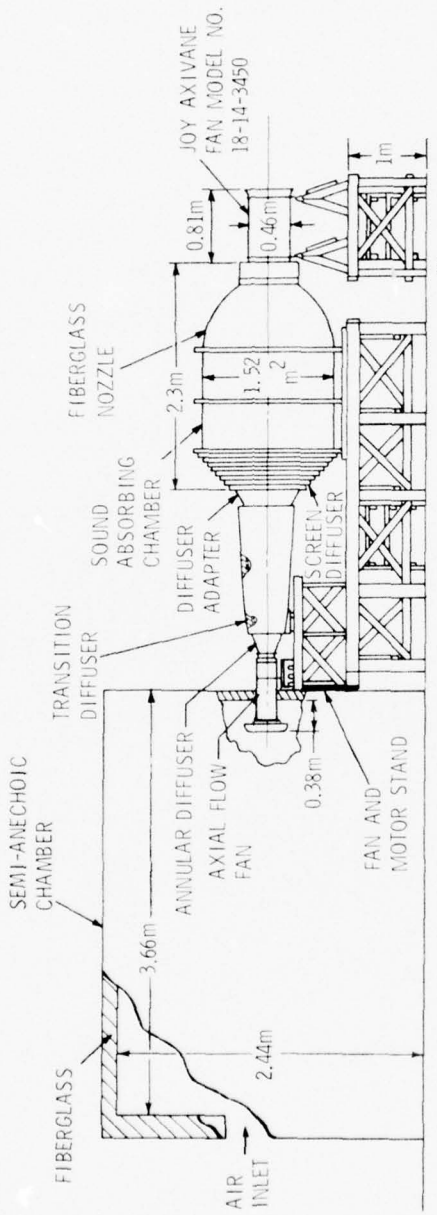

Figure 1. Turbomachinery Noise Facility and Semi-Anechoic Chamber.

vibration isolation units and enclosed inside a plaster board and plywood walled room which has a lead foil sheathing on the outer facing. Certain modifications had to be made to the chamber in order to use it with the rest of the aeroacoustic facility. A removable panel was made for the lead-sheathed outer room to permit the rotor assembly to be as near as possible to the semi-anechoic chamber. A hole, which is plugged with fiberglass when not in use, was made in the wall of the chamber. The hole permits the insertion of the inlet ducting of the rotor into the chamber. A set of fiberglass panels prevents the drawing in of air or noise around the inlet duct. To minimize the ingestion of vortices from the walls of the chamber, the inlet was centered in the wall, protruding 0.38 m into the chamber. The entire facility had to be put on a raised platform in order to center the inlet in the wall. The Joy axial flow fan was placed on a separate platform and connected to a baffle chamber by a rubber gasket to minimize its vibration. In the wall opposite the inlet, a 1.4 m circular hole was cut to permit the flow of air through the chamber. A sheet of porous plastic foam was stretched across this opening to keep dust out of the semi-anechoic chamber and to diffuse the flow.

The semi-anechoic chamber was tested for free-field acoustic conditions. Initial tests before the modifications outlined above showed the chamber to be in good agreement with the inverse square law from 0.1 to 20 kHz. Since this study was concerned with the conditions along the center line of the inlet and there had been substantial modifications, the chamber was tested again for anechoic conditions with

the same results. For a detailed outline of the calibration procedure and a discussion of results, see Appendix A.

3.1.2 Test Rotor and Inlet Duct. A photograph of the rotor is shown in Figure 2. The hub-to-tip ratio of the rotor blades is 0.482. The tip diameter of the rotor is 17.53 cm. The hub diameter is 8.74 cm. The blade profile at three different spanwise locations and the corresponding inlet and exit angles are shown in Figure 3. The blade chord and stagger angle varied over the span as listed in Table I.

TABLE I

ROTOR CHORD AND STAGGER ANGLE VARIATION WITH RADIUS

Radius (cm)	Chord (cm)	Stagger Angle (radians)
4.57	3.99	0.31
5.08	3.94	0.38
5.59	3.99	0.46
6.10	4.04	0.54
6.60	4.06	0.61
7.11	4.09	0.66
7.62	4.09	0.72
8.13	4.11	0.77
8.64	4.14	0.81

The standard configuration of the rotor employed seventeen blades. This gives a mid-span spacing of 2.428 cm. The rotor was also operated with ten blades, with a mid-span spacing of 4.128 cm. The design advance ratio of the seventeen bladed rotor is 2.35 which corresponds to a flow coefficient (ϕ) of 0.75. The range of velocities of the inlet flow at midstream was from 39 to 51.2 m/sec. The rotor was operated in air at 5440 rpm. Figure 2 shows the rotor used in the test program

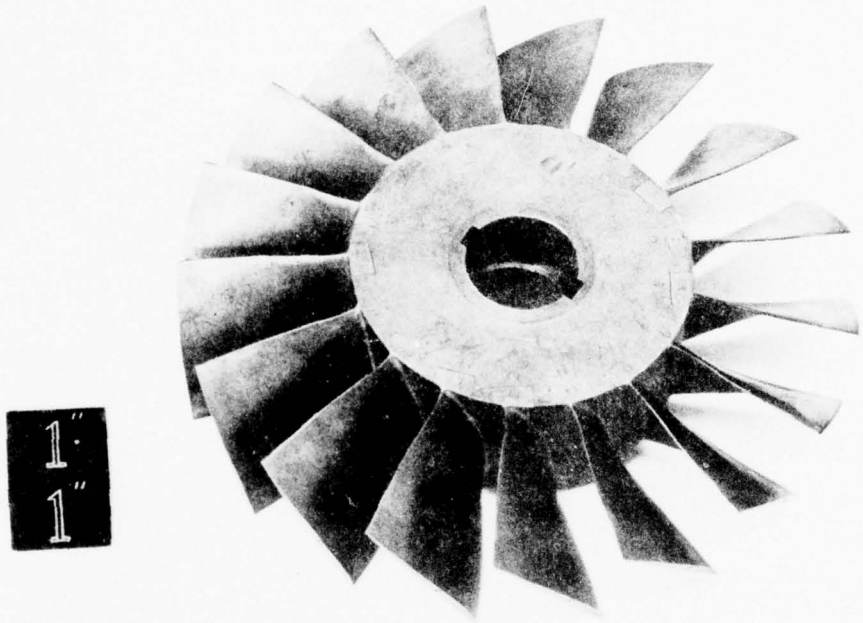

Figure 2. Seventeen Bladed Test Rotor.

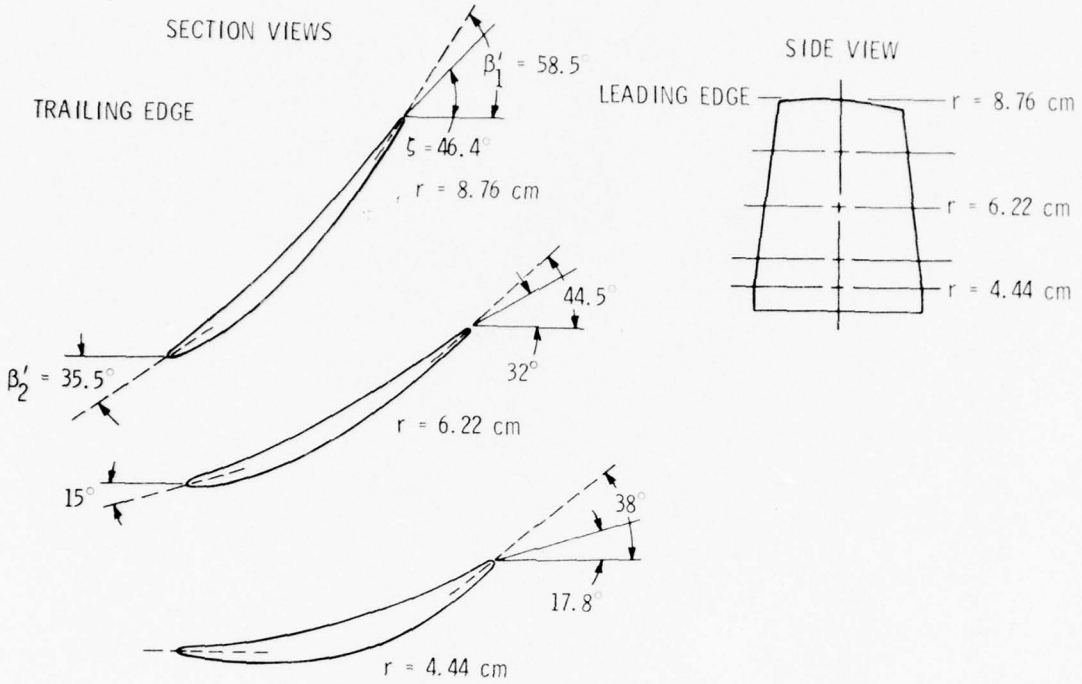

Figure 3. Blade Profiles at Three Radii.

equipped with seventeen blades. In Appendix B, a summary of the steady state aerodynamic response of the seventeen bladed rotor is given.

Because of the desire to study boundary layer turbulence, the inlet duct was extended 0.45 m to permit the formation of a boundary layer. The hub was made longer and stationary. It is supported by six aerodynamically shaped struts, symmetrically located. After much discussion and experimentation, it was found that a coating of rough sandpaper 25.4 cm long on the hub and removal of the nose cone provided a fully developed boundary layer. An artificial boundary layer formed by tripping with a 0.318-cm thick o-ring placed around the hub immediately downstream of the nose cone was also investigated. A description of various other flows and how they were generated is given in Appendix C.

3.1.3 Baffle Chamber and Screen Diffuser. As the flow leaves the rotor, it passes through an annular diffuser before going into the screen diffuser and baffle chamber. The screens allow a tremendous diffusing of the flow without separation before entry to the baffle chamber. The baffle chamber prevents noise from the downstream Joy fan from propagating upstream. It was constructed of six parallel, airfoil shaped baffles inside a 1.52 m by 1.52 m cross section duct. The airfoils, as well as the chamber walls, were lined with 5.0 cm thick fiberglass. For further details of the design and construction, see Robbins [24].

3.2 Experimental Procedure and Instrumentation

3.2.1 Inlet Configurations. The three boundary layers studied were generated by altering the inlet configuration. The axial mean velocity and subsequently the flow coefficient were controlled by the Joy axial flow fan located downstream of the rotor as shown in Figure 1. The natural boundary layer was the result of the original modified inlet. A cross-section is shown in Figure 4(a). An artificial boundary layer was generated by tripping the boundary layer near the inlet opening with a 0.318-cm thick rubber o-ring on the hub, as shown in Figure 4(b). A fully developed boundary layer was formed by coating part of the hub with rough sandpaper and removing the nose cone, as shown in Figure 4(c). The level and structure of the inlet turbulence were altered by placing a square mesh grid at the inlet 3.5 diameters upstream of the rotor. The grid has a mesh size of 2.86 cm and a rod diameter of 0.556 cm. All three cross-sections in Figure 4 are shown with the grid in place. The measurements were also carried out without the grid. In Appendix C, a brief outline describing the developmental work that led to the final inlet configurations and other flows produced is presented.

3.2.2 Aerodynamic Flow Measurements. Flow measurements were taken with x-array hot wire probes. The mean axial velocity, the turbulence intensity and the turbulence integral scales were measured. The axial and tangential components of the turbulence were determined using the linearized King's Law equations for a two sensor hot wire probe as described by Von Frank [25]. Equation (3.1) is for the

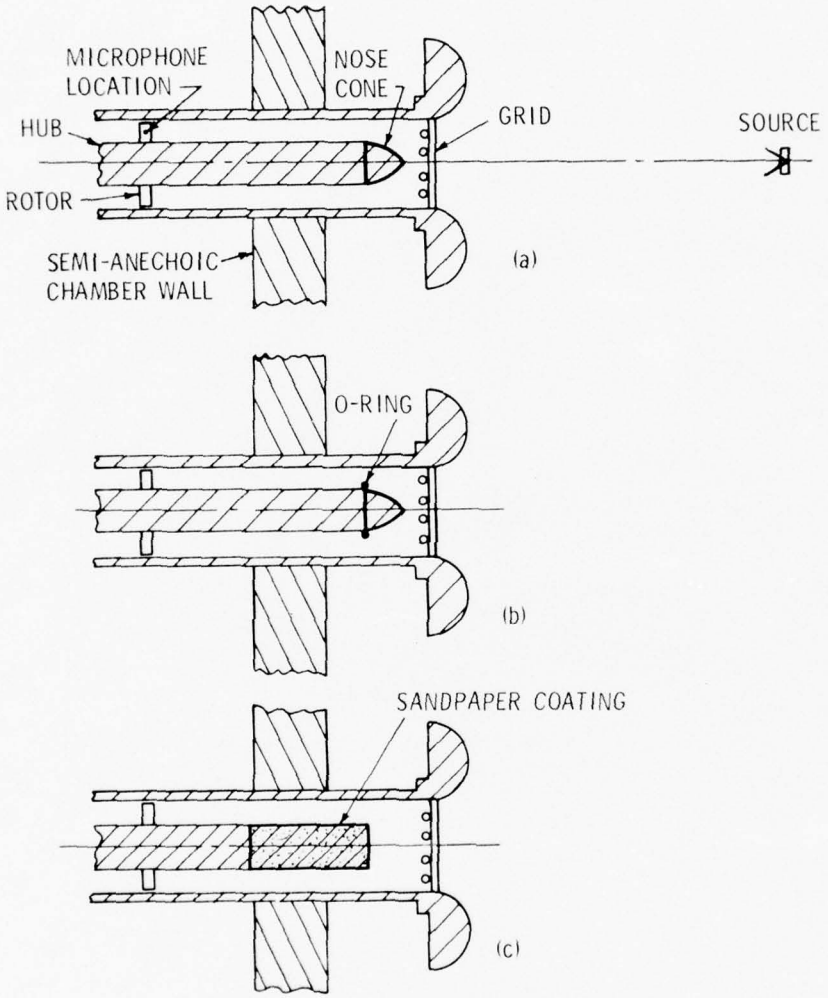

Figure 4. Boundary Layer Duct Configurations: (a) Natural Boundary Layer, (b) Artificial Boundary Layer, (c) Fully Developed Boundary Layer.

axial component of the turbulence velocity fluctuations. Equation (3.2) is the tangential component:

$$\sqrt{\overline{u^2}} = \frac{2\bar{E}\sqrt{U_x}}{F\sqrt{\sin\gamma}} \sqrt{\overline{(e_1 + e_2)^2}} \tag{3.1}$$

and

$$\sqrt{\overline{v^2}} = \frac{2\bar{E}\sqrt{U_x}}{F\sqrt{\sin\gamma}} \sqrt{\overline{(e_1 - e_2)^2}} \quad , \tag{3.2}$$

where

$\sqrt{\overline{u^2}}$ = axial turbulent velocity fluctuations,

$\sqrt{\overline{v^2}}$ = tangential turbulent velocity fluctuations,

E = DC part of anemometer voltages (the same for both sensors),

e_1, e_2 = AC part of anemometer voltages,

F = slope of King's Law equation for sensors in use $(E_1 + e)^2 = E_0^2 + F\sqrt{\overline{V}}$,

γ = angle between sensor and axial direction (= 45°)

and V = velocity normal to the wire.

The calibration curve for each set of two sensors were made identical by electronic manipulation of one sensor's signal. Before, during and after each set of measurements, the sensors were checked for drift from calibration conditions and the necessary corrections, if any, were made.

A diagram outlining the instrumentation for the flow measurements is given in Figure 5. For turbulence intensity and axial mean velocity measurements, the probe was traversed radially along the blade span.

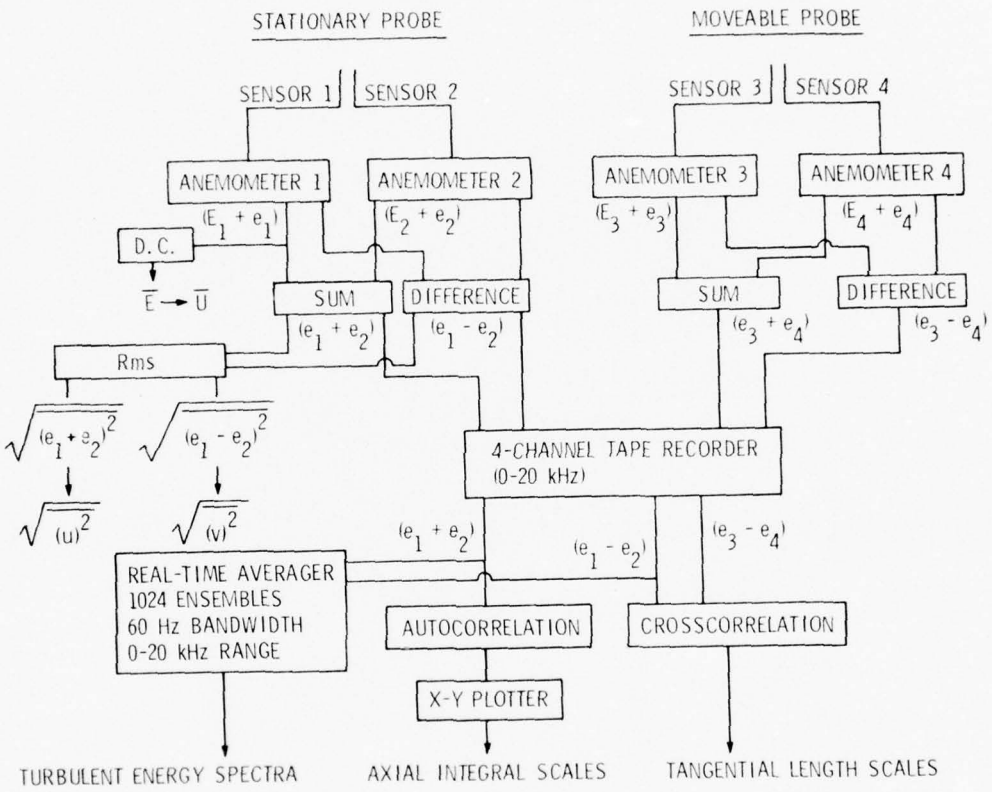

Figure 5. Diagram of Flow Instrumentation.

Measurements were taken at various radial locations at an axial position two chords upstream of the rotor as shown in Figure 6. A brief check was made at two other circumferential positions for symmetry of flow at 90 and 180 degrees angular separation from the main measuring station. The flow was found to be axisymmetric.

The axial integral length scales were determined by recording the output from an x-array, two sensor hot wire probe with a magnetic tape recorder having a frequency range of 0 to 20 kHz at a speed of 30 in/sec. The axial component was then played back through a correlation function computer which has a frequency response down to 0.16 Hz. The resulting auto-correlation curve was recorded on paper by an x-y plotter, see Figure 5. An integral time scale, T, was calculated by integrating the auto-correlation curve:

$$T = \int_0^\infty \rho_{uu}(\tau)\, d\tau \quad , \tag{3.3}$$

where

$$\rho_{uu}(\tau) = \overline{u(x, r, \theta, t)\, u(x, r, \theta, t + \tau)} \; / \; \overline{u^2}$$

The axial integral length scale was found by multiplying the integral time scale by the mean axial velocity at that radial location.

The tangential length scales were measured using two x-array hot wire probes placed at the same radial locations but whose angular separation could be varied, see Figure 7. The tangential components of the anemometers' output signals were recorded on magnetic tape as outlined above for the axial length scales. The cross-correlation of

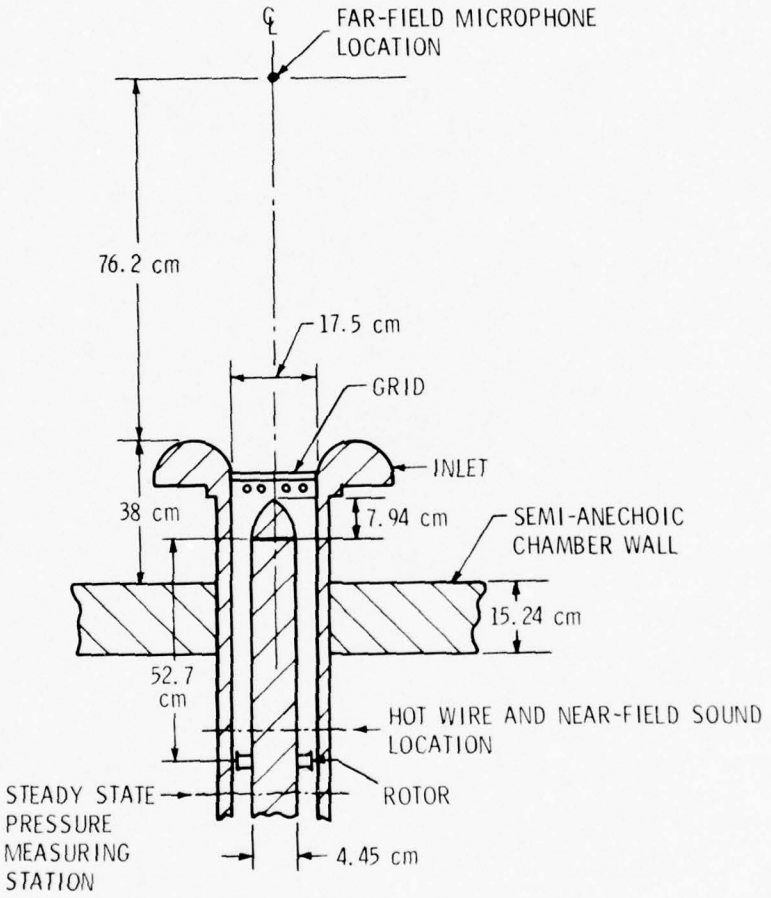

Figure 6. Plan View Showing Measuring Stations.

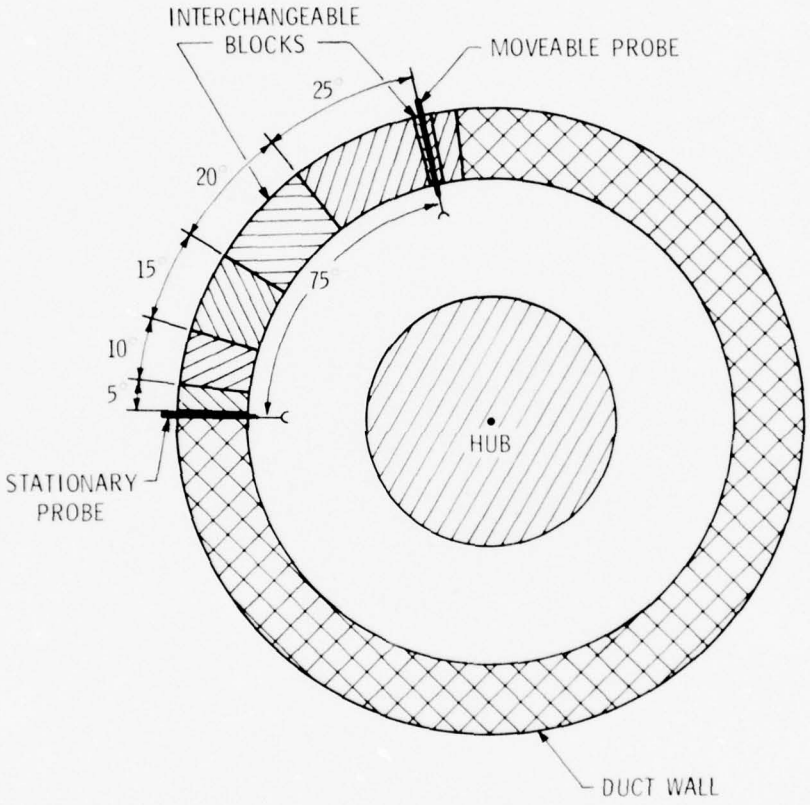

Figure 7. Diagram Showing Two Probe Configuration for Determining Tangential Length Scales.

the recorded output was computed by the correlation computer for several different angular separations at zero time delay. The results were plotted as the cross-correlation coefficient versus angular separation. The tangential integral length scales were computed directly from the curves using Equation (3.4):

$$L_\theta = r \int_0^{2\pi} \rho_{vv}(\theta)\, d\theta \quad , \tag{3.4}$$

where

$$\rho_{vv}(\theta) = \overline{v(x, r, \theta, t)\, v(x, r, \theta + \Delta\theta, t)} \;/\; \overline{v^2} \quad .$$

The axial and tangential integral length scales were determined at five radial locations for all three boundary layers. In addition, the turbulent energy spectra were obtained for both components by passing the recorded components of the anemometer output through a real time analyzer which averaged the signals over 1024 ensembles from 0 to 20 kHz with a 60 Hz bandwidth.

3.2.3 Acoustic Measurements. Measurements of the radiated sound were made at two locations: the near field, two chord lengths upstream of the rotor flush to the inside of the duct wall; and the far field, 4.35 duct diameters upstream of the duct inlet inside the semi-anechoic chamber, as shown in Figure 6. The sound spectra were obtained from the magnetic tape recorded output of a quarter-inch microphone which was filtered through a real time analyzer with a range of 0 to 5 kHz with a 15 Hz filter bandwidth after averaging over 1024 ensembles. The real time analyzer output was recorded on paper by an x-y plotter.

Sound spectra were obtained for the seventeen bladed rotor at three different flow coefficients for the natural boundary layer without the grid. Sound spectra for both the seventeen and ten bladed rotors were obtained for all three boundary layers with and without the grid at the design flow coefficient. All far-field spectra were taken on the center line of the rotor. No directional or sound power measurements were made.

There was concern over the effect of the inlet duct on the radiated sound because of the great length of the duct. Accordingly, calibration of the acoustic response of the duct was performed. The results of the duct calibration are presented and discussed in Appendix D. No corrections of the sound spectra due to duct effects were incorporated in the acoustic spectra of the rotor presented in the next chapter.

CHAPTER IV

DISCUSSION OF EXPERIMENTAL RESULTS

In Table II, a summary of the experimental variables and operating conditions along with the blade passing frequency (BPF) tone sound pressure level (SPL) is presented. The operating conditions for both the seventeen and ten bladed rotors were 5440 rpm with a flow coefficient of 0.75, except for the first two tests listed which were at the flow coefficients of 1.03 and 0.871, respectively. The table includes a descriptive name for the boundary layer, the number of blades of the rotor employed, the maximum mean axial velocity, the SPL of the BPF tone and the SPL of the broadband noise at 2 kHz. A detailed discussion of the flow and acoustic measurements follows.

4.1 Results of Aerodynamic Flow Measurements

The results of the mean axial flow velocity measurements for the three boundary layers are shown in Figure 8. The artificial boundary layer (ABL) as shown is nearly as thick as the natural boundary layer (NBL) but has a much steeper gradient at the hub. The fully developed boundary layer (FDBL) is much thicker than either the ABL or NBL. Figure 9 is a plot of the logarithm of the velocity ratio U_x/U_c against the logarithm of nondimensional distance from the hub, y/r_t. A straight line can be drawn through each series of points belonging to an individual boundary layer. The slope of each line is different, showing that each boundary layer has a different shear stress. The straight

TABLE II

SUMMARY OF BOUNDARY LAYERS AND FAR-FIELD ACOUSTIC MEASUREMENTS

Number of Blades	Boundary Layer	Grid	Flow Coefficient	U_c m/sec	Far-Field			
					10 Blade BPF Tone Level SPL	17 Blade BPF Tone Level SPL	2 kHz SPL	
							10 Blade	17 Blade
17	Natural	No	1.03	51.5	----	79.0	----	65.5
17	Natural	No	0.871	43.5	----	79.0	----	60.3
10, 17	Natural	No	0.75	39.0	81.4	79.0	58.4	59.3
10, 17	Natural	Yes	0.75	39.0	79.4	74.7	58.1	61.2
10, 17	Artificial	No	0.75	39.9	79.0	79.9	56.1	60.9
10, 17	Artificial	Yes	0.75	39.9	74.4	74.2	58.4	62.6
10, 17	Fully Developed	No	0.75	39.5	84.7	82.7	66.9	65.0
10, 17	Fully Developed	Yes	0.75	39.5	75.3	80.0	63.3	64.0

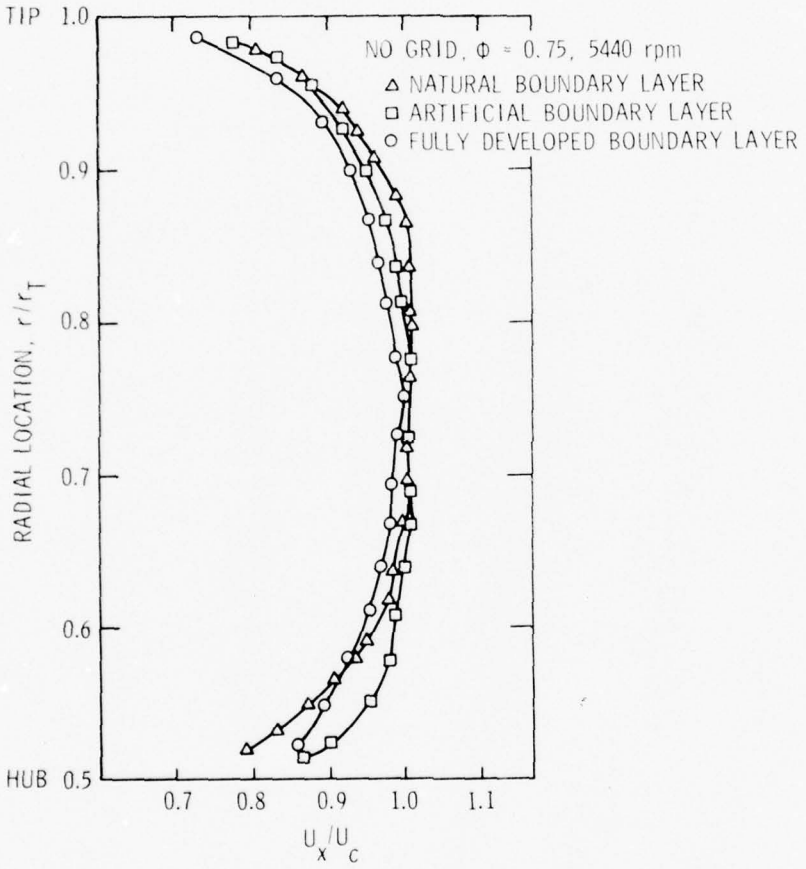

Figure 8. Mean Velocity Profiles - With and Without Grid.

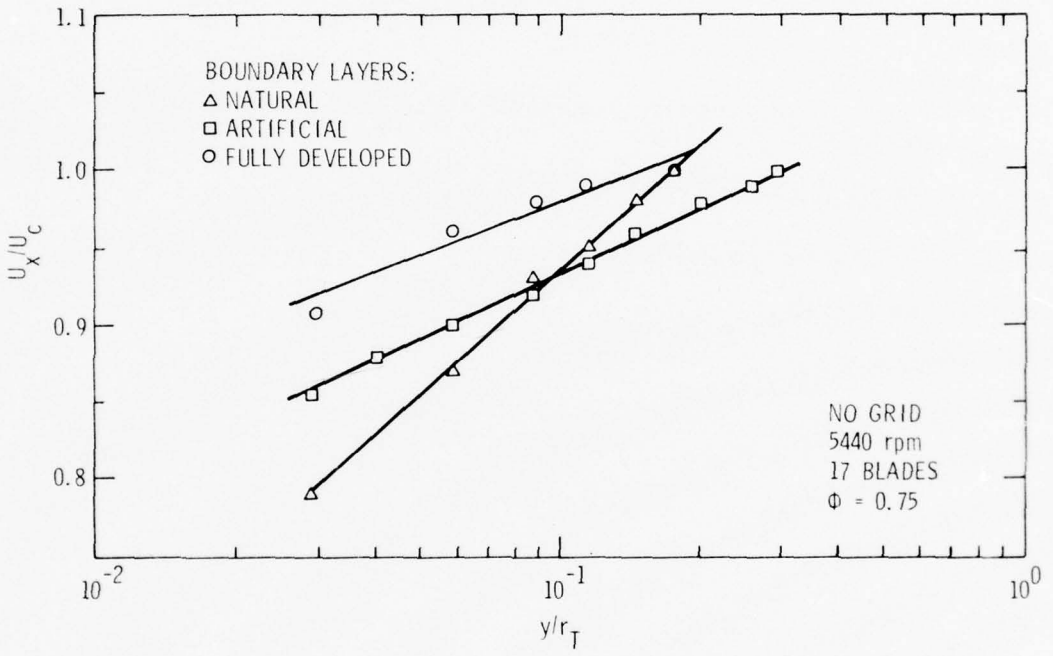

Figure 9. Law of the Wall Plots.

lines drawn through the points indicate that the boundary layers are conventional in nature.

In Figures 10 and 11, the turbulence intensity profiles are plotted with and without the grid installed for all three boundary layers. The turbulence intensities increase with increasing boundary layer thickness, with maximum intensities occurring for the FDBL case. The turbulence intensities with the grid installed are generally higher. For the NBL, the tangential component is much lower than the axial component. For the ABL and FDBL, the two components of turbulence intensities are nearly the same for the middle third of the passage. The tangential component is still the lesser of the two. Hanson's [18] data indicates that, for a fan operating in atmospheric turbulence, the contraction at the inlet results in a higher tangential component of turbulence intensity ($v'/u' \approx 3$) than the axial component. In the present investigation, the eddies are contracted as they are sucked through an opening in the wall of the anechoic chamber, as shown in Figure 1, allowed to expand inside the chamber and contracted a second time at the inlet to the fan. This could account for the discrepancies between Hanson's measurements and those presented here.

For the axial component of the turbulent velocity fluctuations, two length scales were found to exist simultaneously with no grid for all three boundary layers. Figure 12(a) is a typical auto-correlation curve with no grid showing evidence of two length scales and how they were defined. This evidence also appears in the tangential spatial-correlations as explained later. While this evidence for two scales

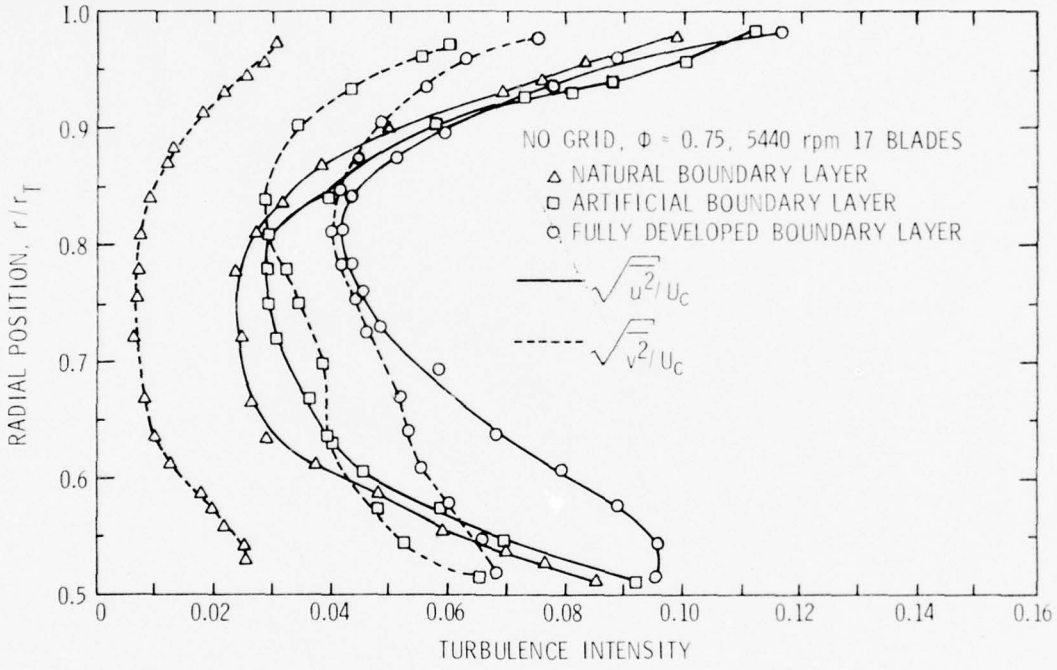

Figure 10. Turbulence Intensity Profiles - No Grid.

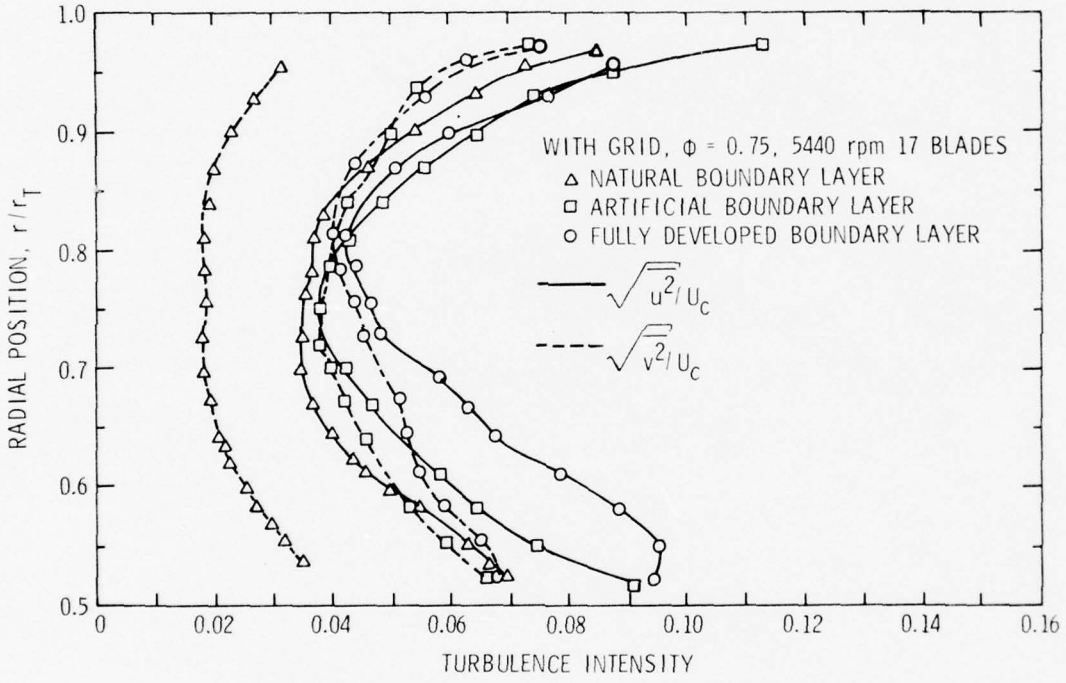

Figure 11. Turbulence Intensity Profiles - Grid.

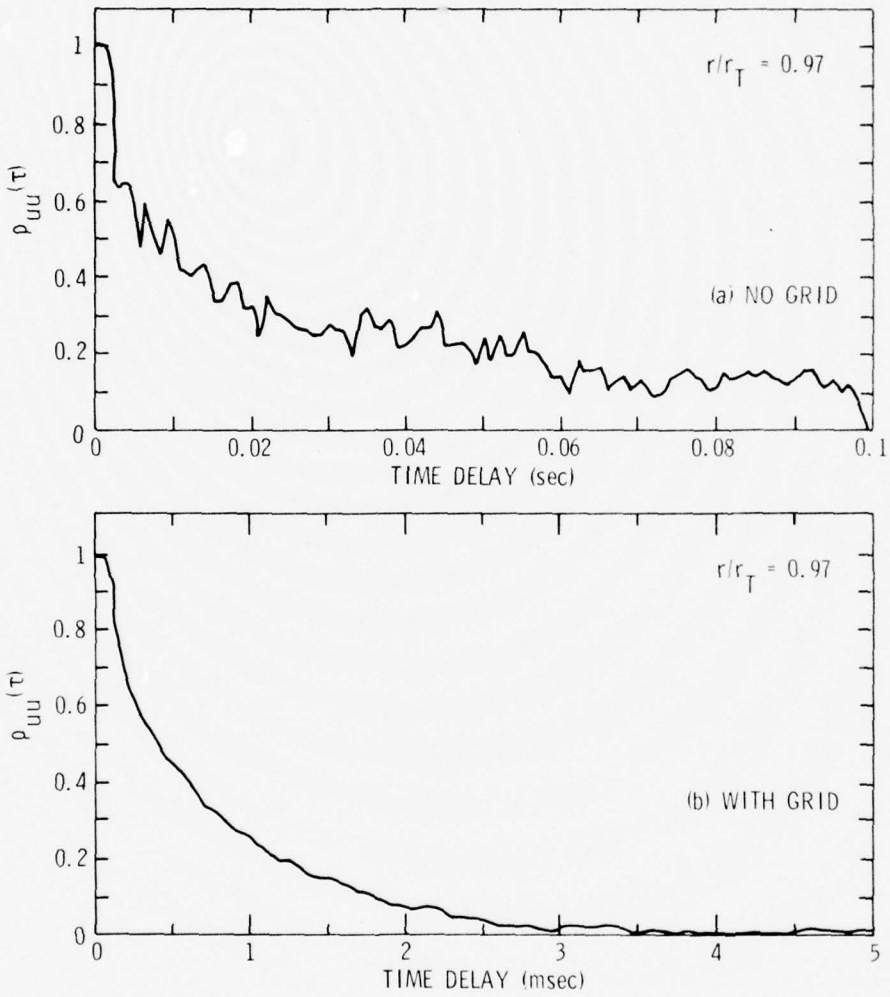

Figure 12. Typical Auto-Correlation Curves for Natural Boundary at ϕ = 0.75, 5440 rpm, Seventeen Bladed Rotor.

TABLE III

AXIAL INTEGRAL LENGTH SCALES

Figures in parentheses are L/S values for 17 blades - to derive L/S for 10 bladed, divide the figures in parentheses by 1.7. N.P. = Not Present

Boundary Layer	r/r_T	No Grid; Long	No Grid; Short	Grid
Natural (NBL)	0.57	85.67 (50.7)	9.60 (5.68)	1.45 (0.86)
	0.61	68.51 (34.7)	6.73 (3.41)	2.25 (1.14)
	0.75	90.51 (37.1)	9.37 (3.84)	1.90 (0.74)
	0.88	97.10 (35.7)	11.80 (4.33)	2.18 (0.80)
	0.97	117.20 (37.3)	5.40 (1.72)	2.24 (0.71)
Artificial (ABL)	0.52	386.1 (228.6)	69.1 (40.9)	1.91 (1.13)
	0.58	120.7 (64.3)	14.2 (7.56)	1.73 (0.92)
	0.70	83.6 (37.1)	13.5 (6.00)	0.871 (0.387)
	0.84	194.3 (67.9)	45.2 (15.8)	1.05 (0.37)
	0.97	152.1 (48.4)	39.4 (12.5)	3.23 (1.03)
Fully Developed (FDBL)	0.52	163.6 (96.9)	21.3 (12.6)	2.10 (1.24)
	0.58	N.P.	2.03 (1.08)	2.11 (1.12)
	0.70	34.5 (15.3)	3.20 (1.42)	1.52 (0.675)
	0.84	N.P.	1.36 (0.47)	0.424 (0.148)
	0.97	84.6 (26.9)	13.3 (4.23)	0.958 (0.305)

persists for the tangential cross-correlation with the grid, it disappears for the auto-correlation as shown in Figure 12(b). This indicates that the grid introduces uniformity into the axial direction but has little effect on the tangential length scale. One reason the grid has little effect on the tangential size of the eddies is that the mesh size of the grid is the same order as the eddy sizes. In addition, the distance of the grid upstream of the rotor permits the formation of eddies in the boundary layer.

In Figures 13, 14 and 15, the auto-correlation curves at five radial locations for all three boundary layers are plotted, both with and without the grid. In Table III, the corresponding integral axial

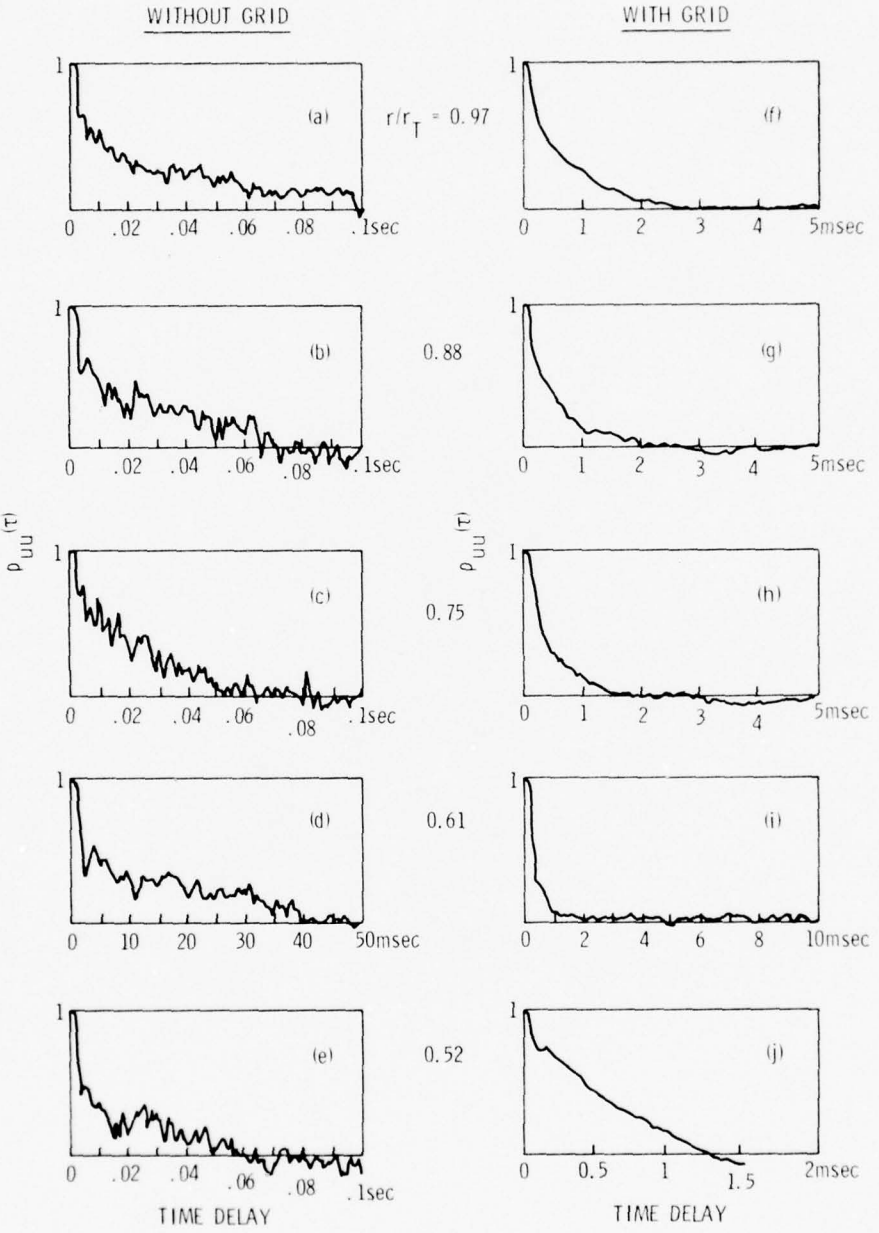

Figure 13. Auto-Correlation Curves for Natural Boundary Layer at ϕ = 0.75, 5440 rpm, Seventeen Bladed Rotor.

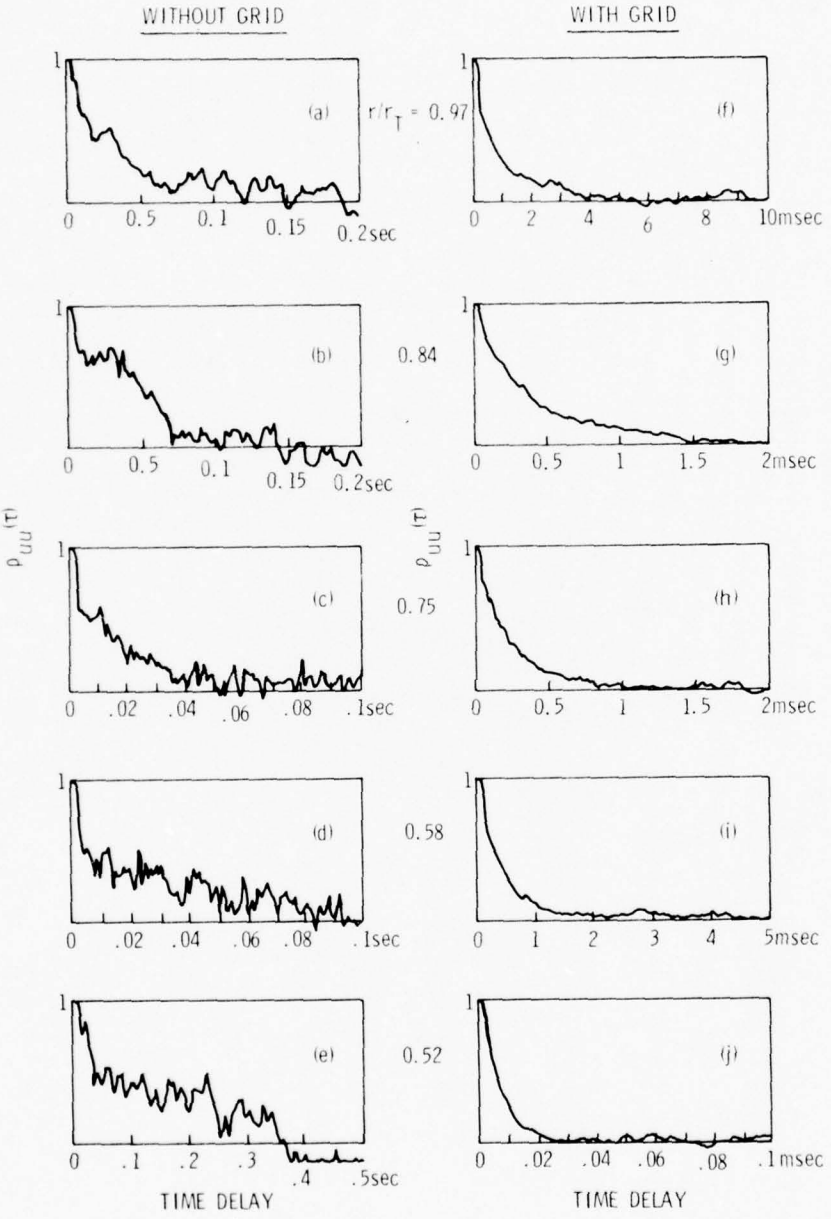

Figure 14. Auto-Correlation Curves for Artificial Boundary Layer at ϕ = 0.75, 5440 rpm, Seventeen Bladed Rotor.

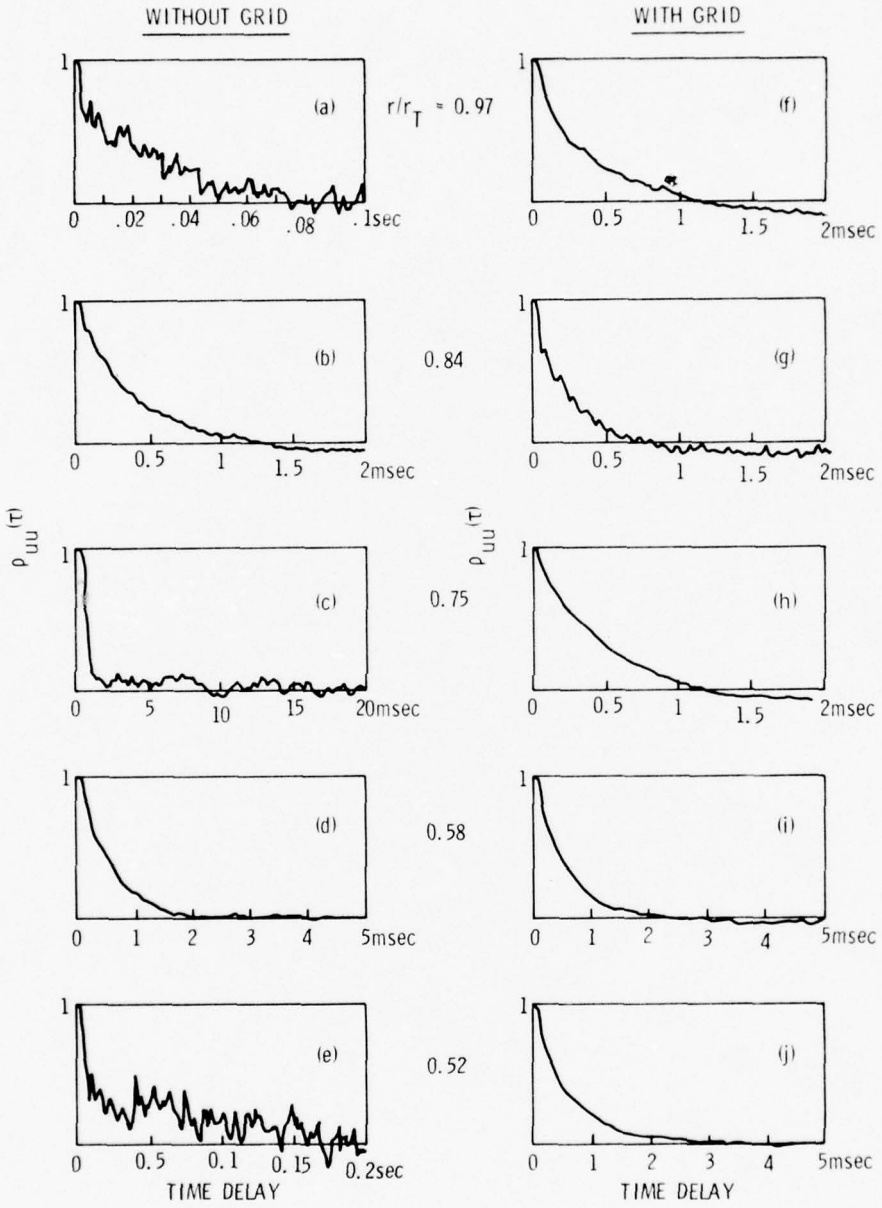

Figure 15. Auto-Correlation Curves for Fully Developed Boundary Layer at ϕ = 0.75, 5440 rpm, Seventeen Bladed Rotor.

length scales as computed from Equation (3.3) are listed along with the ratio of length scale to blade spacing. Two length scales are present at each location in each boundary layer with no grid, except for the FDBL which has only one scale at two of the five locations listed. There is always just one scale with the grid installed. The method used to generate the FDBL, i.e., removal of the nose cone, may be responsible for generating the short eddies.

The NBL shows the greatest uniformity for axial length scales with no grid installed. The FDBL shows the greatest variation. These variations are smoothed out by the installation of the grid and the axial scales have the same order of magnitude for all three boundary layers.

Table IV gives the average integral length scales. These scales were also derived using Equation (3.3), as previously discussed. However, instead of splitting the auto-correlation curve into two parts as shown in Figure 12(a), the entire auto-correlation curve was integrated.

In Figures 16, 17, and 18, the spatial cross-correlation curves are plotted for five locations for the three boundary layers, with and without grid installed. The plots for the NBL and FDBL are similar at all radial locations. The ABL is radically different. At three radial locations, the correlation becomes negative. This indicates a second eddy with velocity fluctuations opposite those of the first eddy. The o-ring used to trip the boundary layer may be introducing a disturbance which has the effect of a phase shift. This contributes to the artificial nature of the boundary layer.

TABLE IV

AVERAGE AXIAL INTEGRAL SCALES - NO GRID

Boundary Layer	r/r_T	Average Axial Length Scale (cm) (No Grid)
Natural	0.52	46.2
	0.61	41.9
	0.75	76.9
	0.88	68.0
	0.97	80.9
Artificial	0.52	321.3
	0.58	73.7
	0.70	54.4
	0.84	160.8
	0.97	112.3
Fully Developed	0.52	112.3
	0.58	2.03
	0.70	4.83
	0.84	1.36
	0.97	69.6

Table V lists the tangential integral length scales derived from Figures 16, 17, and 18 using Equation (3.4). Two length scales were present at all locations, with and without the grid; however, not all could be computed. This is because the plots do not always tend to zero as the angle of separation approaches infinity, see Figure 17.

The explanation for the two length scales found in this investigation is as follows. There are two different sources of turbulence involved. The first is atmospheric turbulence present in the anechoic chamber. As the room sized eddies are ingested into the inlet, they are stretched, resulting in very long and narrow eddies. Hanson [18] found the same effect. In his study, Hanson found an L_x of over 30 m

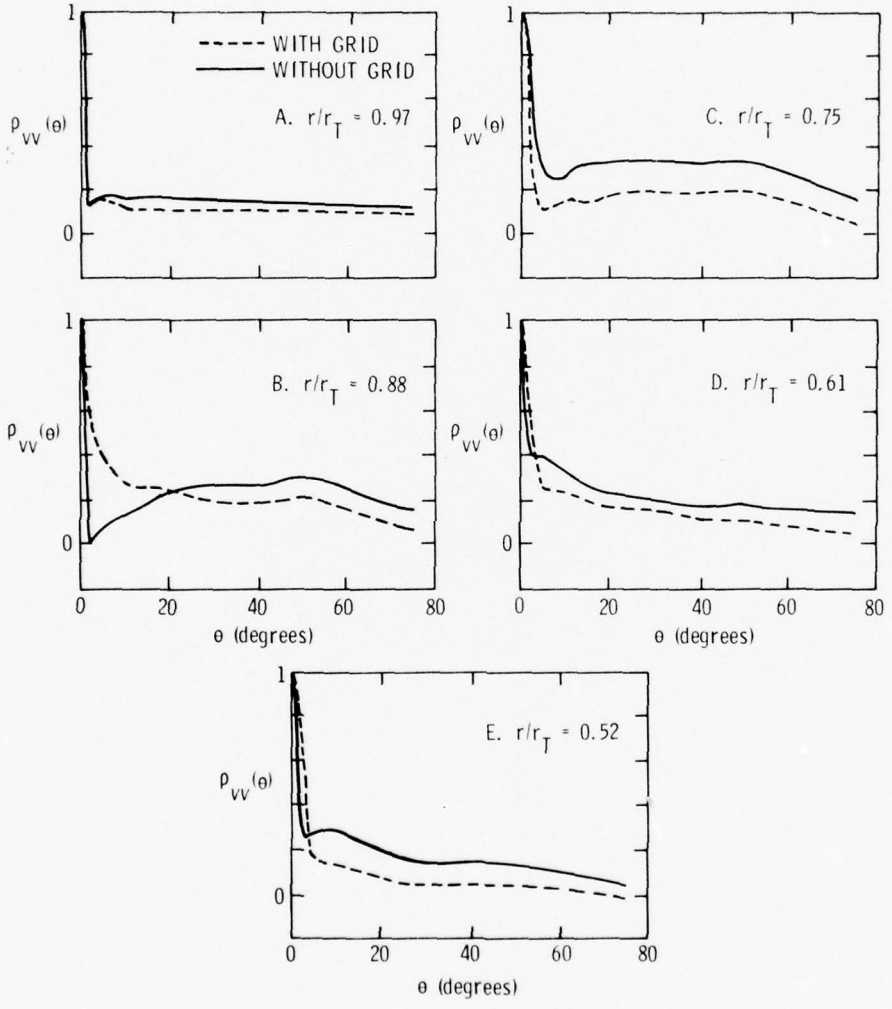

Figure 16. Cross-Correlation Curves for Natural Boundary Layer at $\phi = 0.75$, 5440 rpm, Seventeen Bladed Rotor.

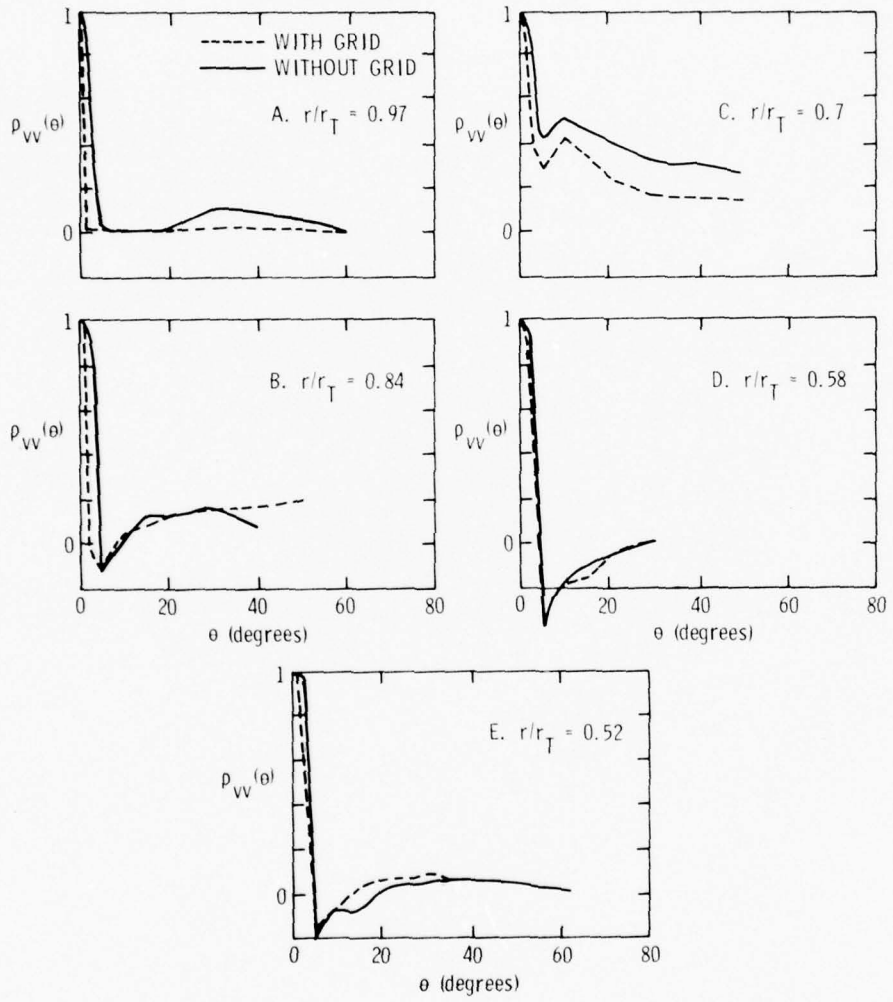

Figure 17. Cross-Correlation Curves for Artificial Boundary Layer at ϕ = 0.75, 5440 rpm, Seventeen Bladed Rotor.

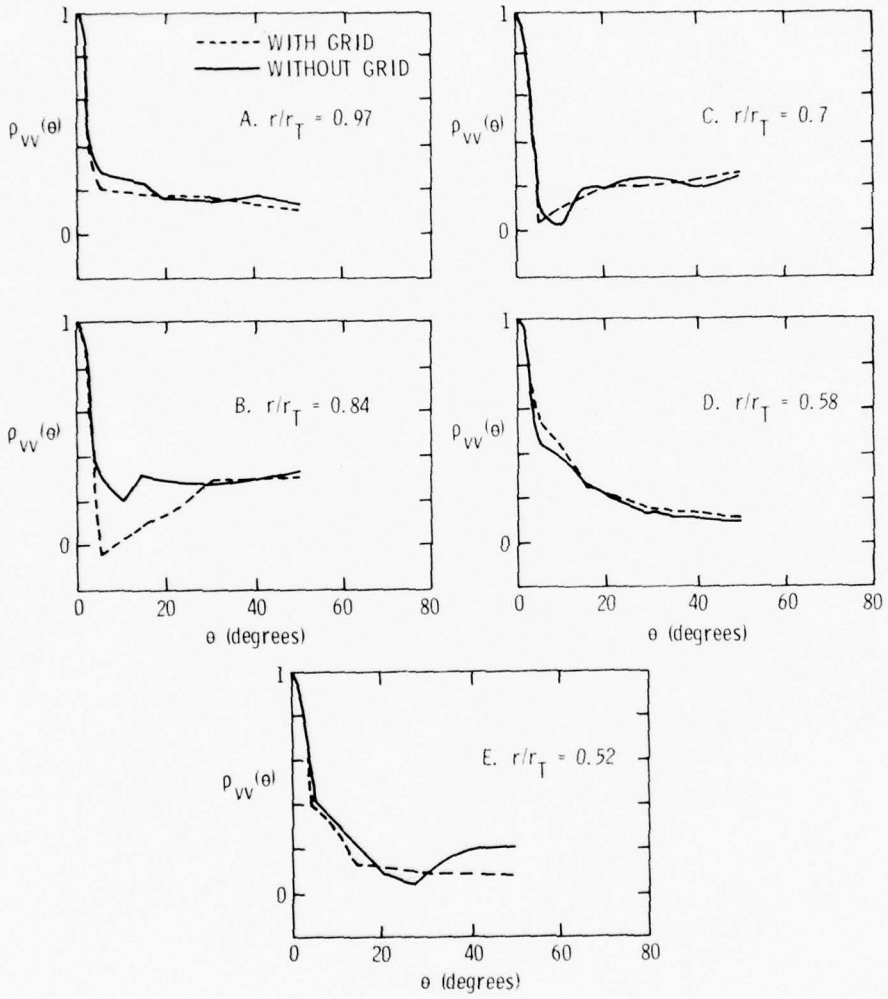

Figure 18. Cross-Correlation Curves for Fully Developed Boundary Layer at $\phi = 0.75$, 5440 rpm, Seventeen Bladed Rotor.

TABLE V

TANGENTIAL INTEGRAL LENGTH SCALES
(cms)

Natural Boundary Layer

Radius	No Grid; Large	Small	Grid; Large	Small
0.52	3.66	0.074	2.16	0.112
0.61	9.27	0.107	7.24	0.155
0.75	7.95	0.178	7.01	0.124
0.88	12.27	0.051	11.18	0.356
0.97	23.37	0.178	8.08	0.178

Artificial Boundary Layer

Radius	No Grid; Large	Small	Grid; Large	Small
0.52	0.500	0.287	0.320	0.213
0.58	0.709	0.290	0.864	0.213
0.70	3.560	0.483	3.100	0.361
0.84	0.323	0.452	0.386	0.170
0.97	4.010	0.391	N.D.	0.147

Fully Developed Boundary Layer

Radius	No Grid; Large	Small	Grid; Large	Small
0.52	1.83	0.348	1.82	0.328
0.58	1.27	N.P.	1.29	N.P.
0.70	N.D.	0.384	N.D.	0.348
0.84	1.17	N.P.	N.P.	0.447
0.97	6.15	0.460	5.64	0.432

N.P. = Not present.
N.D. = Not determinable.

with an L_θ of only 7.6 cm. In this study, the long L_x, averaged over the blade span, is 90 cm while the short L_x is 8.6 cm for the natural boundary layer case. The average L_θ was 10.4 cm for the large and 0.12 cm for the short. Hanson found a longer L_x primarily because he started with larger eddies. The upper limit is the size of the semi-anechoic room, while Hanson's limit was the planetary boundary layer.

The second set of length scales, short L_x and large L_θ, are generated in the boundary layer. This is the primary reason the grid had little effect on the tangential scales. The eddy exists in the form of a ring vortex. In the ABL, this vortex appears to have changed its direction of rotation. This is probably due to the trip ring used near the nose of the hub.

The energy spectra of the axial and tangential components of the turbulence were also measured at five radial locations for each boundary layer with and without the grid. Normalization of the spectra levels by the total turbulence intensity of that component at that radial location for a particular boundary layer collapses them into the narrow bands shown in Figure 19. The slope of both components is -2.6 in the range of wavenumbers, 10 to 100 m^{-1}.

4.2 Results of Acoustic Measurements

Figure 20 shows typical sound spectra with the corresponding background levels for the FDBL with grid, the case with the smallest change in level between background and rotor noise level. The background noise is 10 dB lower than the rotor noise at all frequencies. Thus, the background noise has no effect on the radiated sound from the rotor.

The results of the sound measurements show a definite dependence on turbulent length scales. In Figures 21 and 22, the sound spectra with and without grid are compared for both the near and far field of the seventeen and ten bladed rotors. The decrease in the number and strength of the BPF harmonic tones is due solely to the great

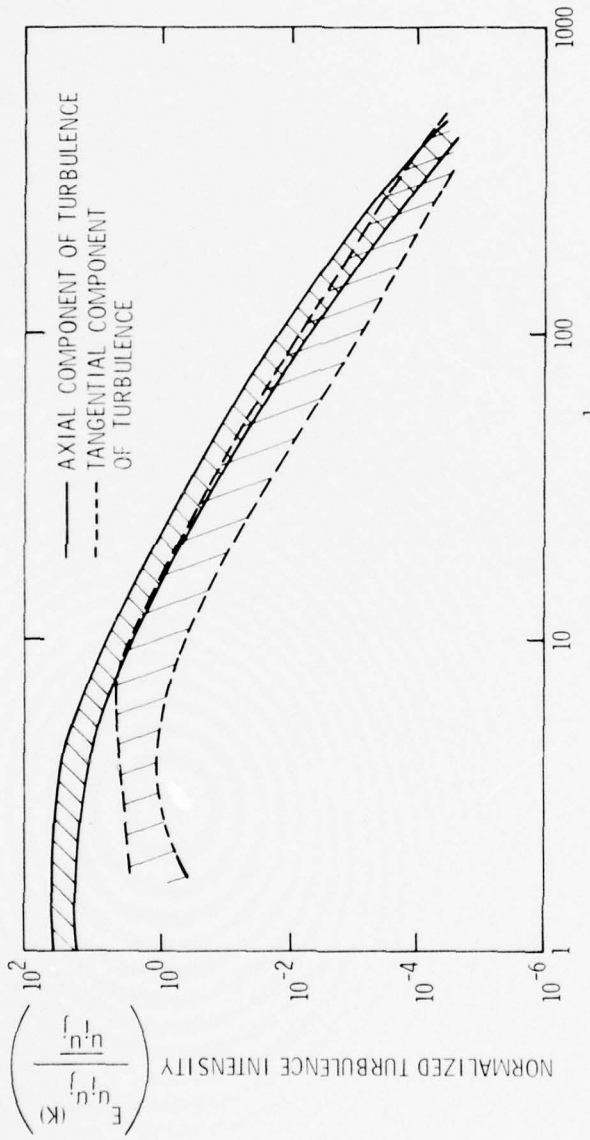

Figure 19. Normalized Turbulent Energy Spectra.

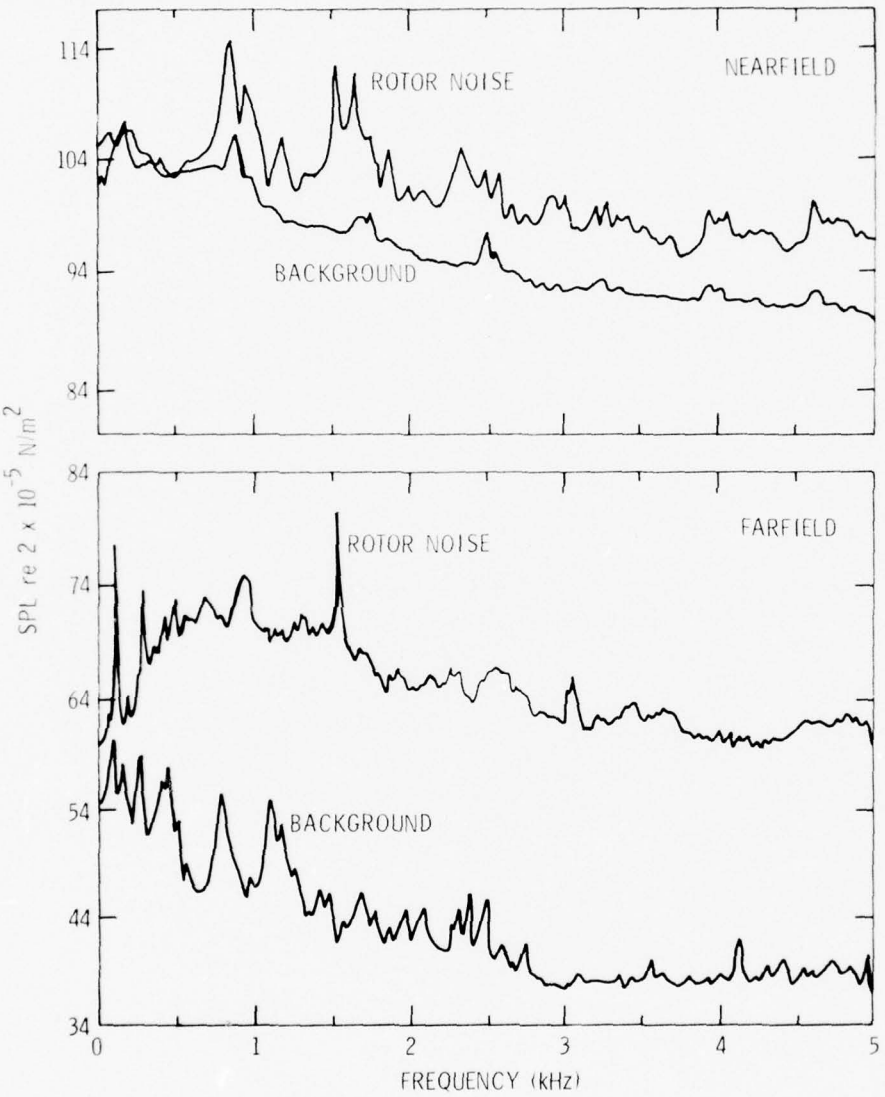

Figure 20. Typical Rotor Noise and Background Levels for Fully Developed Boundary Layer with Grid, $\phi = 0.75$, 5440 rpm, Seventeen Bladed Rotor.

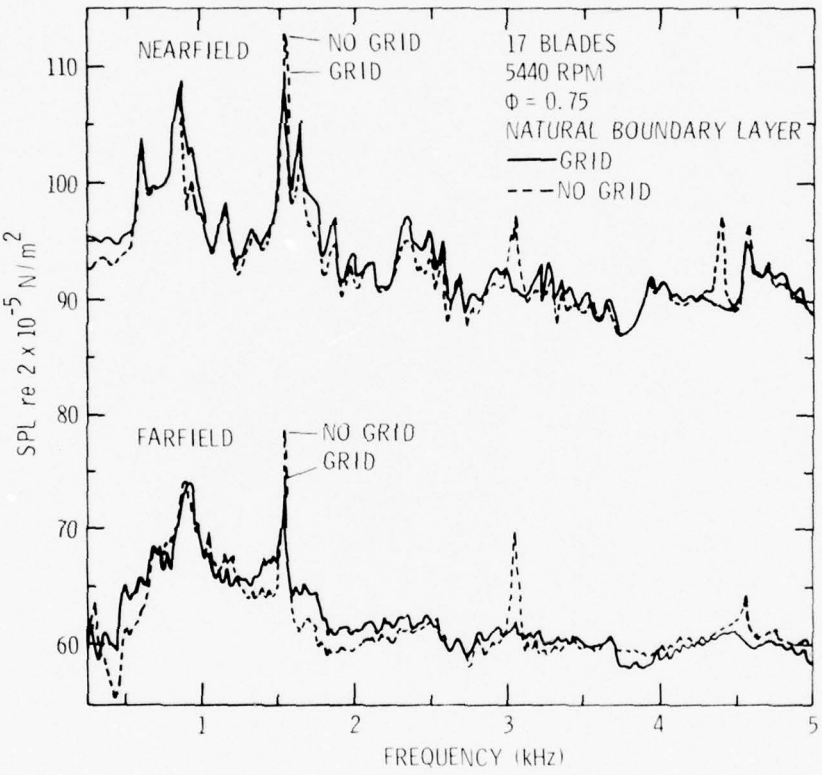

Figure 21. Seventeen-Bladed Rotor Sound Spectra - Near and Far Field.

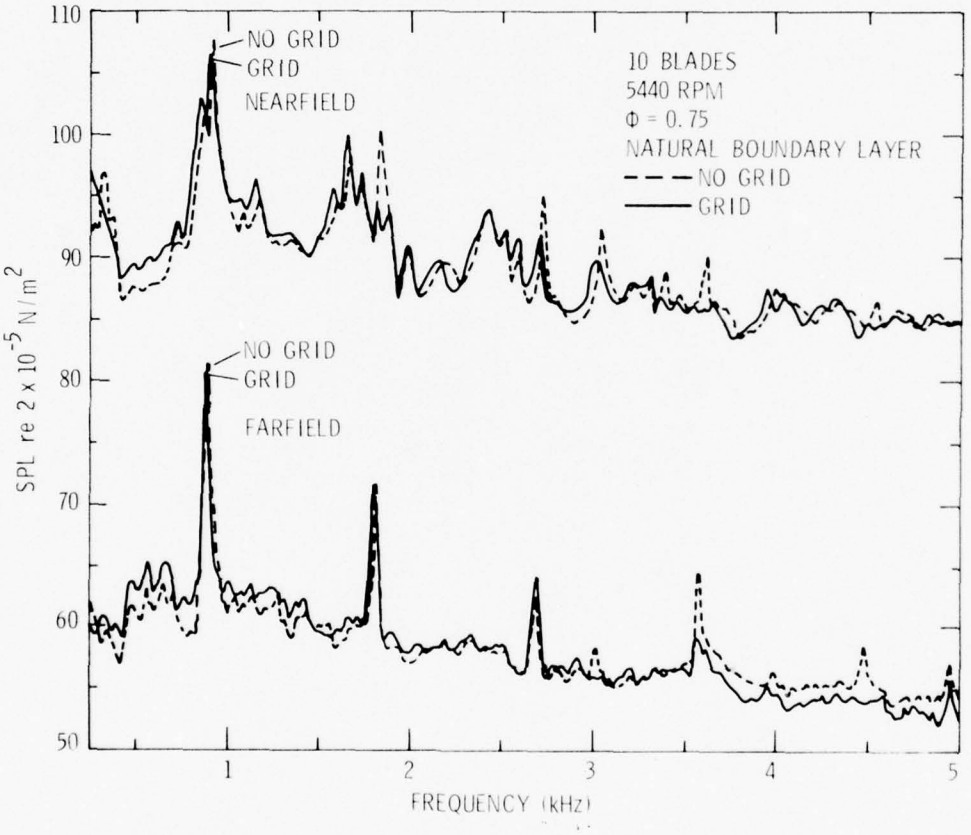

Figure 22. Ten-Bladed Rotor Sound Spectra - Near and Far Field.

decrease in axial length caused by installation of the grid. The small rise in broadband noise is attributed to the increase in turbulence intensity due to the presence of the grid.

In order to compare directly the sound spectra of the seventeen and ten bladed rotors, the spectra must be normalized to the same scale. Frequency is normalized using the nondimensional parameter, $f/B\Omega$, where f is the frequency, B is the number of blades and Ω is the rotor rps. The turbulence properties were measured only for the seventeen bladed rotor and assumed to be identical for the ten bladed rotor, since the operating and blade geometries are the same for both rotors. Hence, the only change in the two configurations is the blade spacing, chord-to-spacing ratio and the steady blade loading. The unsteady aerodynamic transfer function is dependent on the spacing and is approximately proportional to the slope of the lift coefficient, C_L, versus incidence curve. Using the flat plate cascade theory, the increase in noise level due to the change in spacing is about 2 dB at BPF. The remaining increase for the ten bladed rotor spectrum is presumably due to the change in the length-to-space ratio, L/S, where L is fixed. The results are compared in Figure 23. They confirm Mani's [4] prediction that, with decreasing L/S, the general noise level rises and the BPF harmonic peaks broaden.

A comparison of the radiated sound spectra for the seventeen and ten bladed rotors operating with all three boundary layers, without and then with the grid are shown in Figures 24 through 31 for the near and far sound fields. A general increase in noise level is associated with

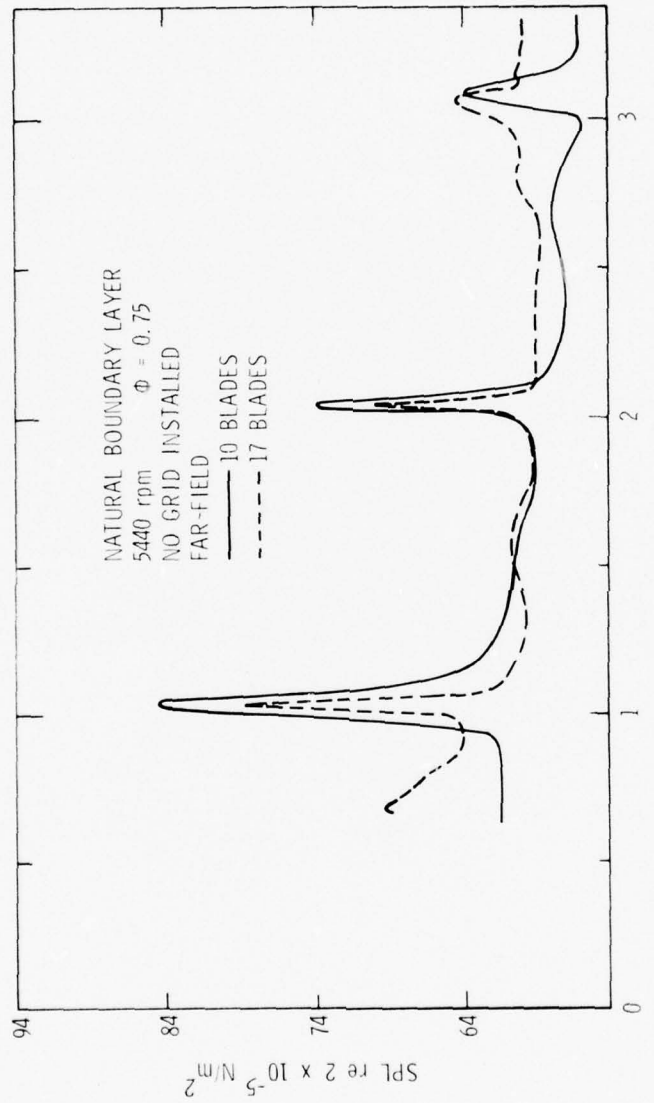

Figure 23. Comparison of Nondimensional Seventeen- and Ten-Bladed Rotor Sound Spectra for Far Field.

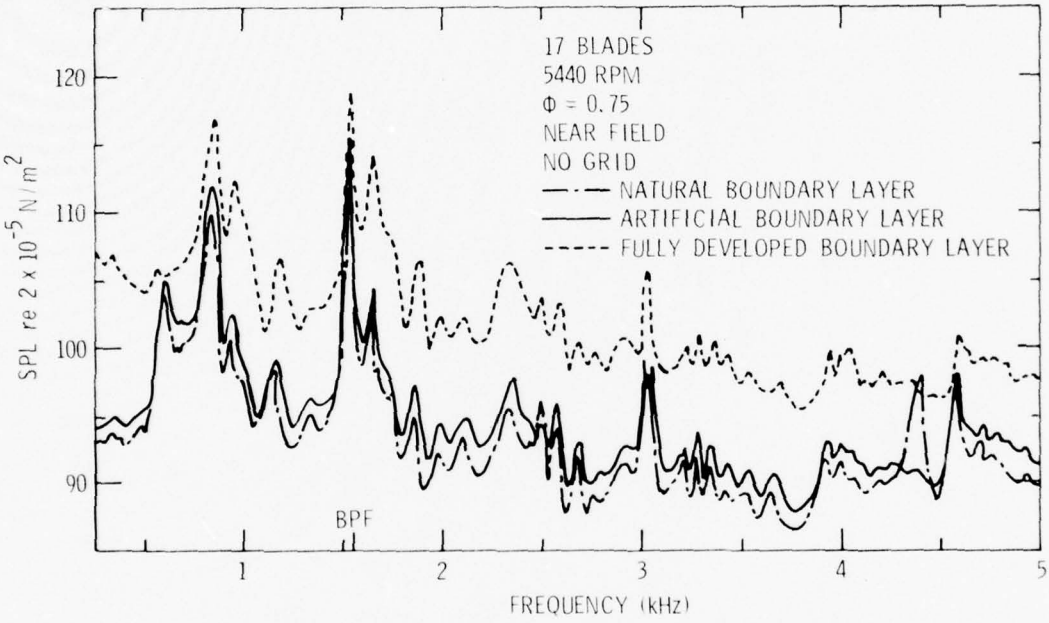

Figure 24. Seventeen-Bladed Rotor Sound Spectra for Three Boundary Layers with No Grid for Near Field.

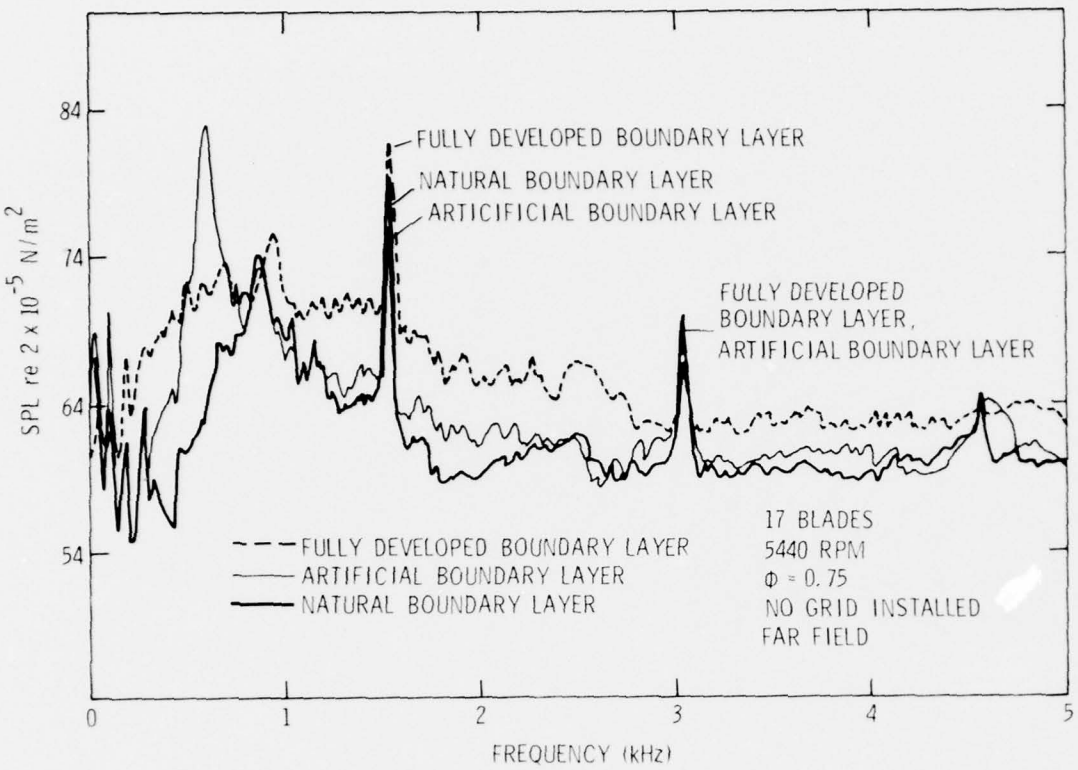

Figure 25. Seventeen-Bladed Rotor Sound Spectra for Three Boundary Layers with No Grid for Far Field.

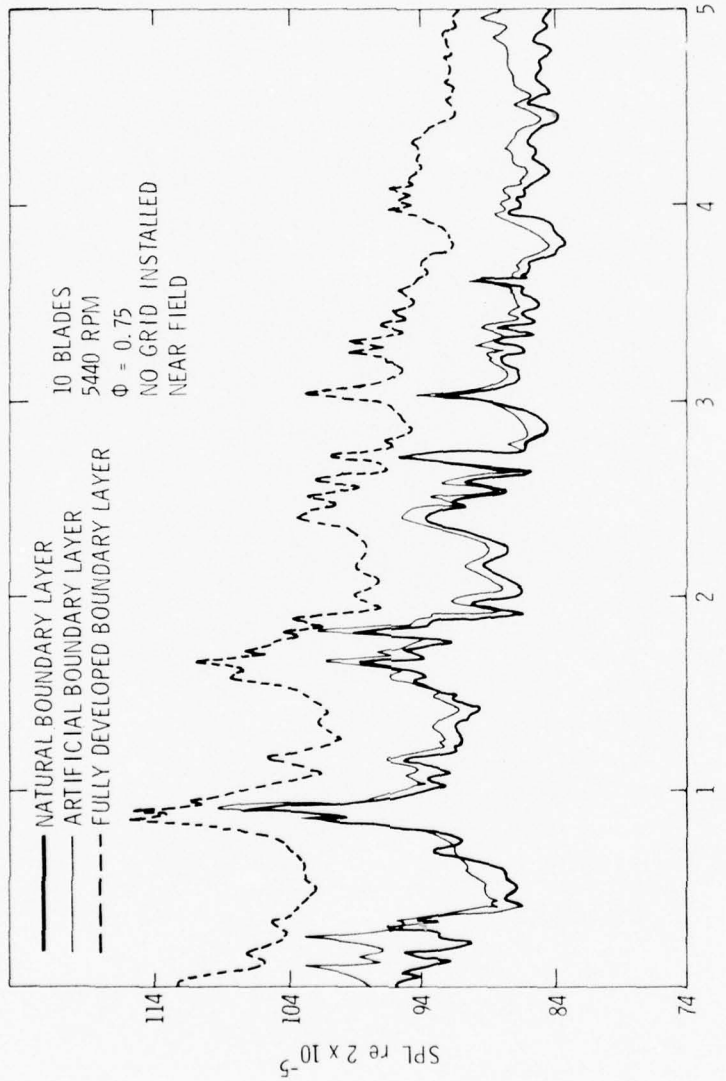

Figure 26. Ten-Bladed Rotor Sound Spectra for Three Boundary Layers with No Grid for Near Field.

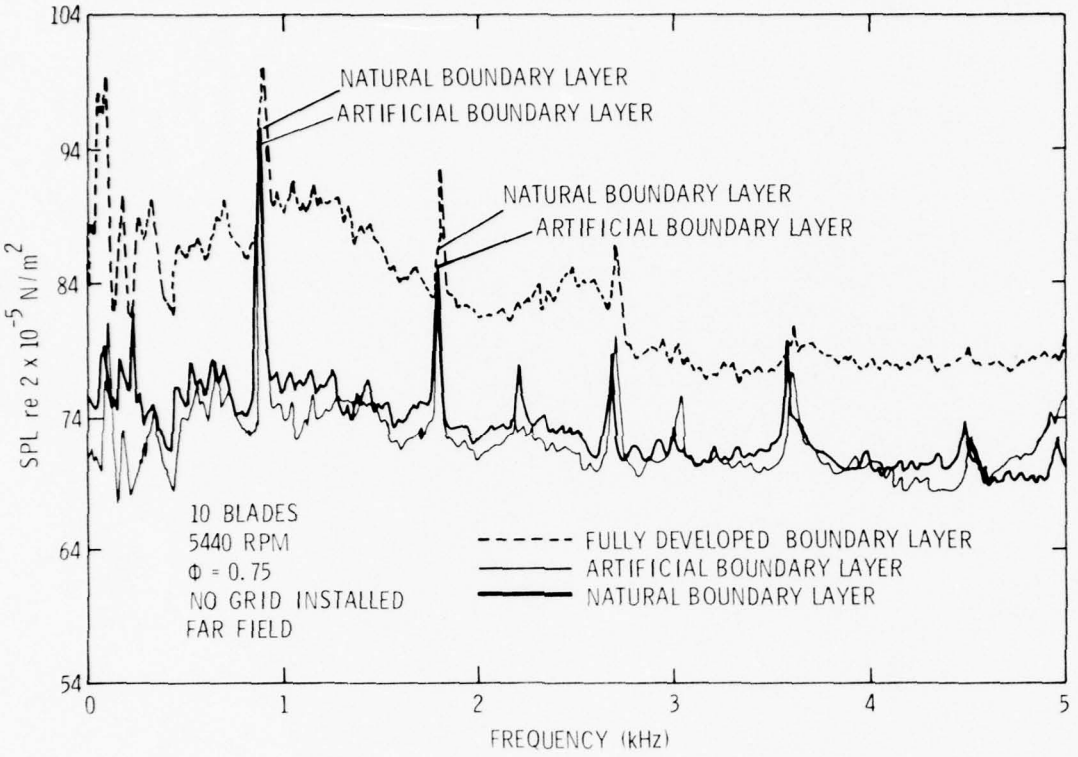

Figure 27. Ten-Bladed Rotor Sound Spectra for Three Boundary Layers with No Grid for Far Field.

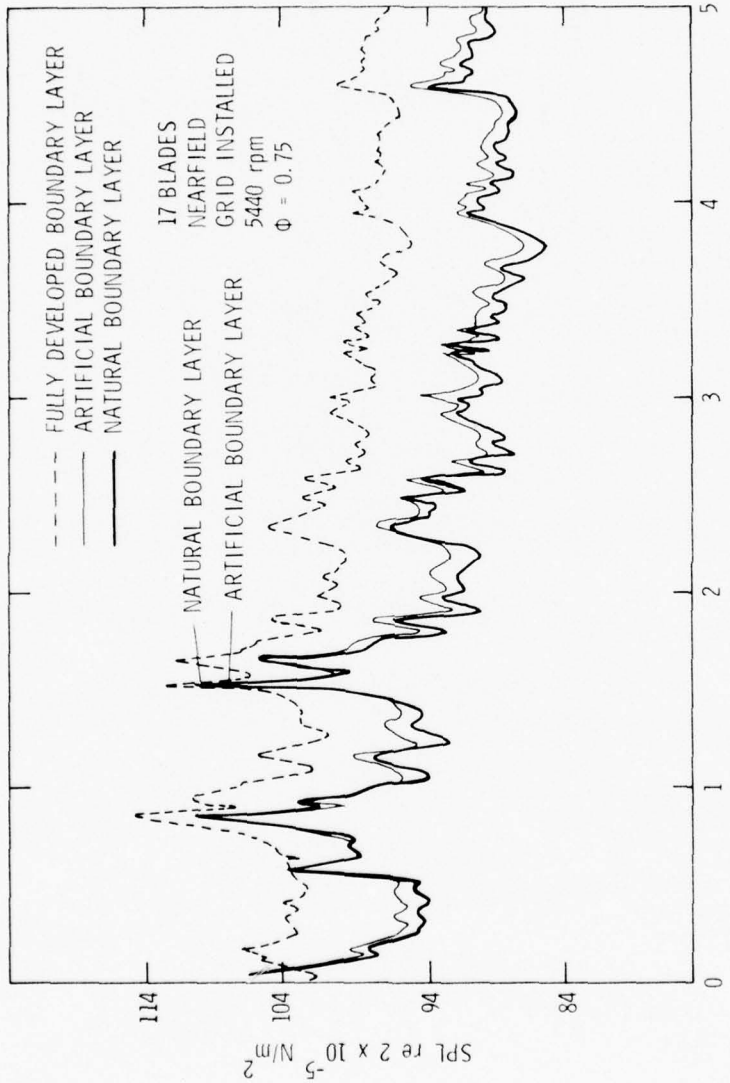

Figure 28. Seventeen-Bladed Rotor Sound Spectra for Three Boundary Layers with Grid for Near Field.

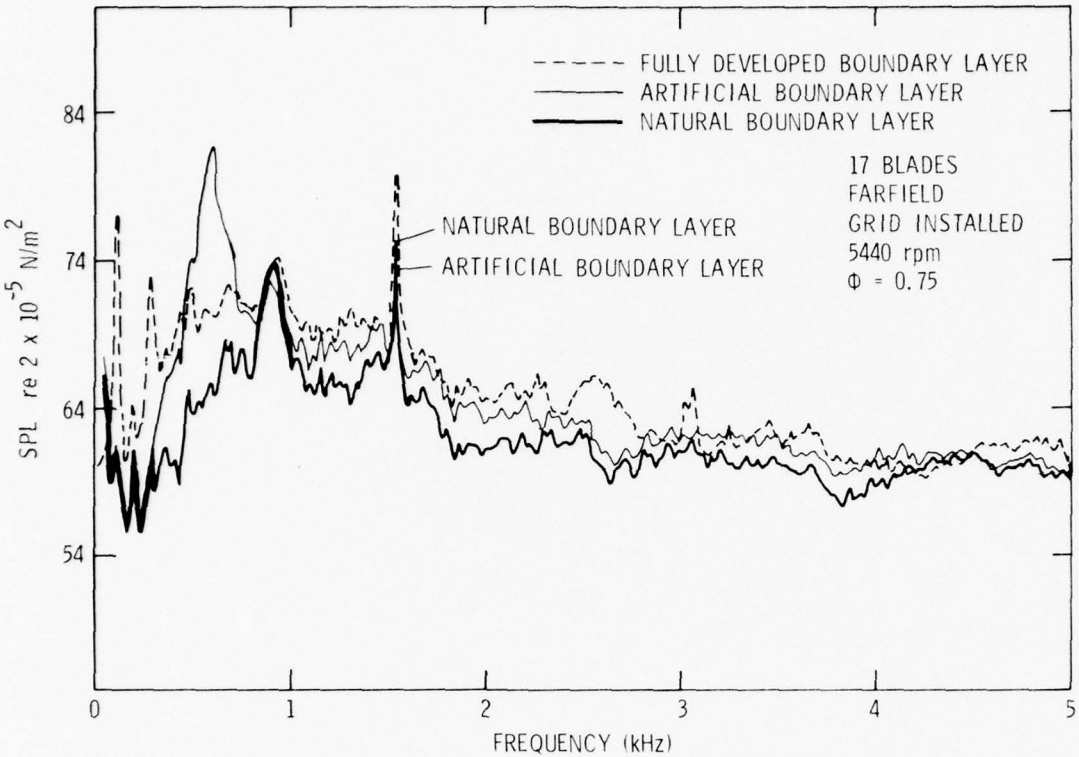

Figure 29. Seventeen-Bladed Rotor Sound Spectra for Three Boundary Layers with Grid for Far Field.

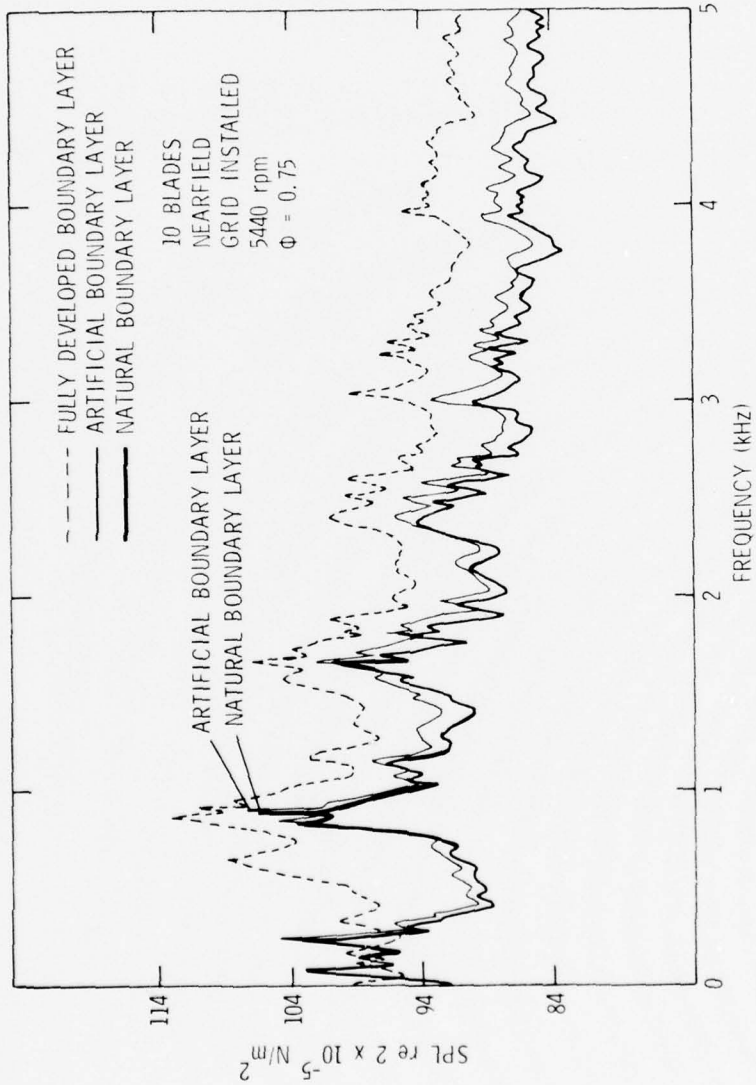

Figure 30. Ten-Bladed Rotor Sound Spectra for Three Boundary Layers with Grid for Near Field.

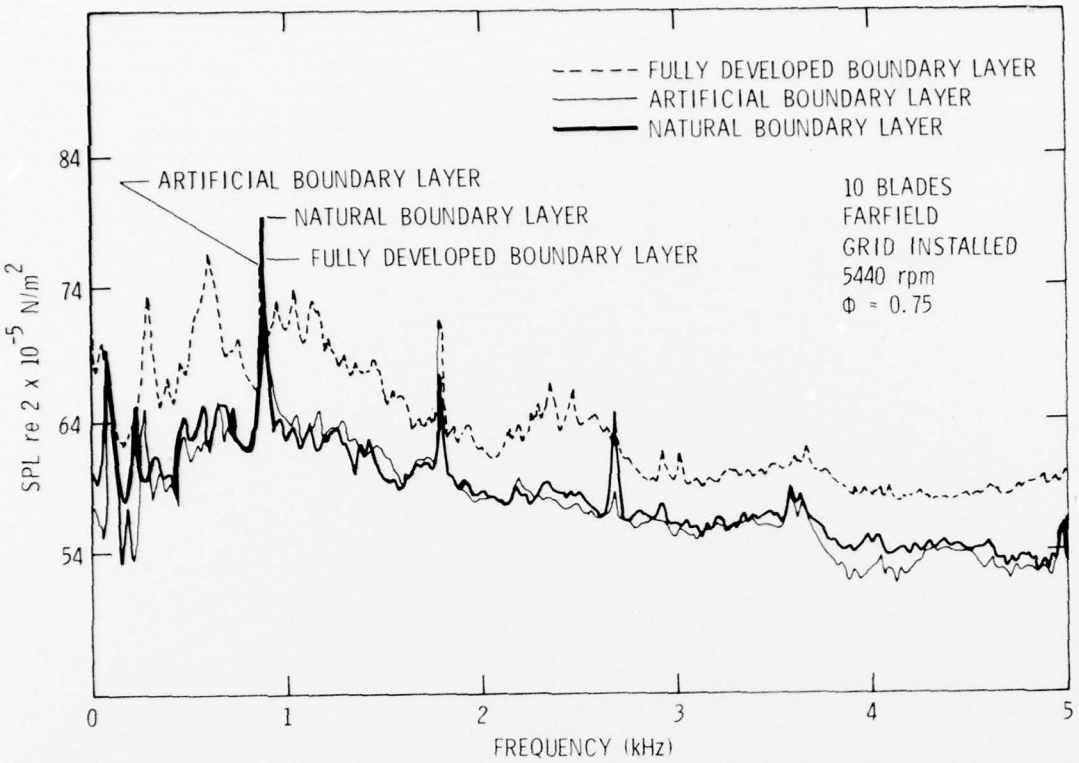

Figure 31. Ten-Bladed Rotor Sound Spectra for Three Boundary Layers with Grid for Far Field.

an increase in boundary layer thickness. Since the slope and shape of the spectra remains the same, depending only on the presence or absence of the grid, no mean velocity gradient or shear stress effects on the radiated sound can be discerned. The general rise in noise level with increasing boundary layer thickness is thus attributed to the increase in turbulence level that is also associated with increasing boundary layer thickness.

The BPF harmonic tones have a different change in sound pressure level between boundary layers than the broadband noise. This is because the BPF harmonic tones have a greater dependence on axial turbulence length scale than the broadband noise has (see discussion on Figures 21 and 22 above). The BPF tone is highest for the fully developed boundary layer. This is a consequence of the much higher levels of turbulence intensity associated with the FDBL. Referring back to Figures 21 and 22 and Table III and the BPF tone levels given in Table II, it is apparent that the axial length scale has more influence on the number and strength of the higher harmonics of the BPF tone than on the strength of the BPF tone itself. Hence, a small difference between the NBL and ABL BPF peaks and the relatively large difference between the FDBL and NBL peaks is seen. The BPF noise seems to be highest for the FDBL case with the ABL being the lowest of the three. Referring to Table II and III, it is evident that the ABL has the longest axial length scale and shortest tangential length scale. The latter may have considerable influence in providing the lowest noise level at BPF for all the cases compared. This seems to indicate

the importance of the ratio of the tangential length scale to blade/spacing (L_θ/S), which is less than unity at most radii for ABL case, on BPF tone level.

There are broadband tonal peaks at frequencies near 800 kHz for several of the spectra shown in Figures 24 through 32. These peaks are still present in repeated tests. The exact source of these tones has not been determined. They appear to be aeolian tones generated by the support structure of the motor which is used to drive the rotor.

Figure 32 shows the sound spectra for the natural boundary layer without grid at three different flow coefficients, 0.75, 0.871 and 1.03. The rise in broadband noise level is due to the increase in mean velocity and turbulence intensity associated with the increased flow coefficient. A decrease in flow coefficient means an increase in steady pressure on the blades. From Figure 32, it is evident that an increase in steady pressure leads to an increase in the number of BPF harmonic tones present in the rotor noise spectrum.

Decreasing the number of rotor blades while keeping the flow coefficient constant increases the steady pressure on the blades. Hence, the spectrum for the ten bladed rotor should have more BPF harmonic tones present than the seventeen bladed rotor. In Figure 33, the sound spectra for both the ten and seventeen bladed rotors are compared for the frequency range 0 to 10 kHz. The ten bladed spectrum has five harmonic tones and the seventeen bladed has four. In addition, the ten bladed higher harmonics are stronger than the seventeen bladed tones. This is further evidence that increasing the steady blade loading increases the number of BPF harmonic tones.

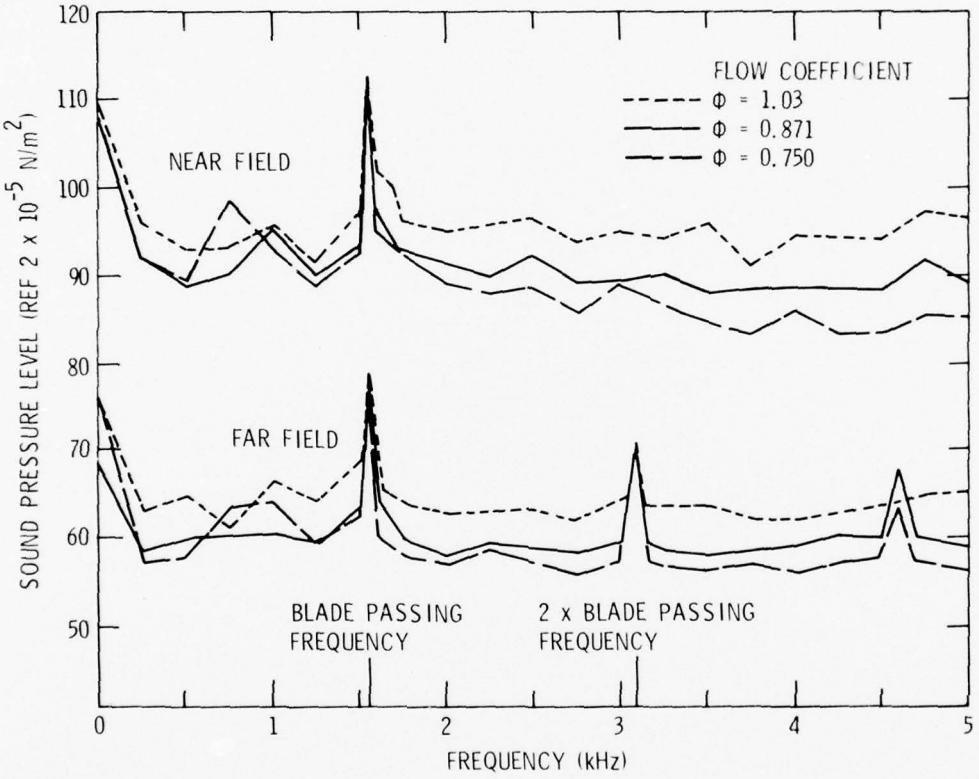

Figure 32. Seventeen-Bladed Rotor Sound Spectra for Three Flow Coefficients for the Natural Boundary Layer with No Grid.

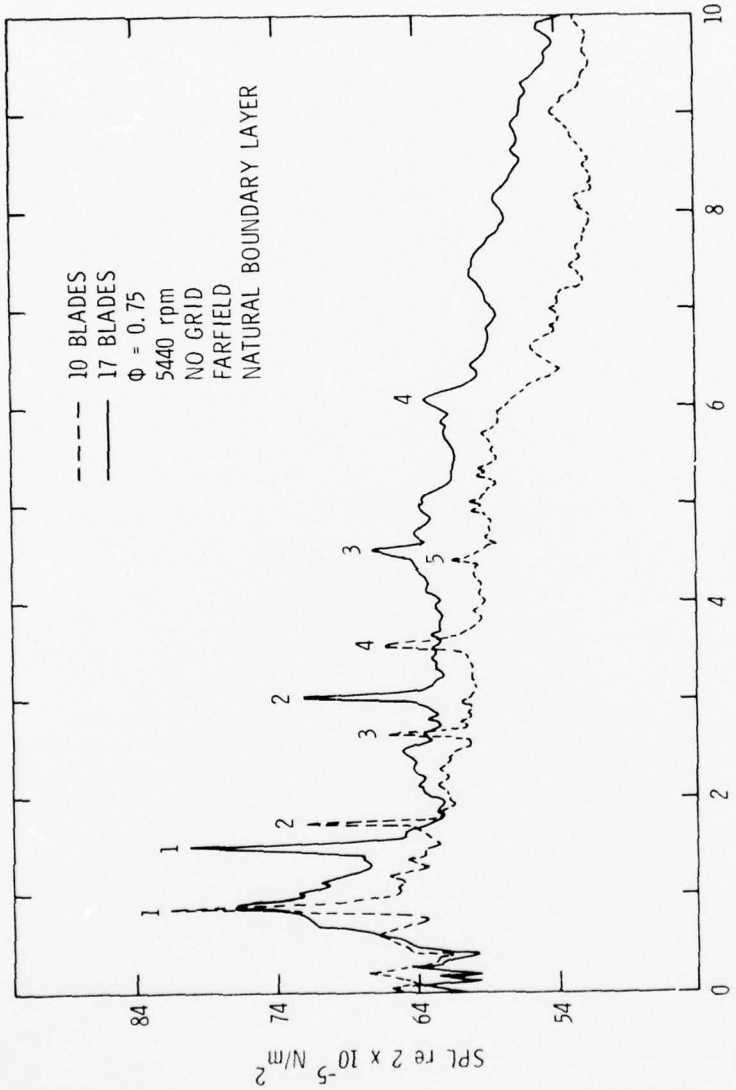

Figure 33. Comparison of Seventeen- and Ten-Bladed Rotor Sound Spectra for Natural Boundary Layer with No Grid for Far Field, 0-10 kHz.

In Figure 34, the time histories for the BPF tone level are shown for the NBL and ABL with and without the grid for the near field. It is evident that the tone levels fluctuate a great deal; however, the range of fluctuation is the same for the no-grid case (long length scales) as it is for the grid case (short length scales). Cumpsty and Lowry [22] observed a marked difference between in-flight BPF tone level fluctuations and those for a static test. This was attributed primarily to the absence of elongated eddies, as found in static tests, for in-flight conditions. In the present test, the grid eliminates long axial length scales and yet the level of fluctuation in the BPF tone was unchanged. The very narrow tangential scales are present for both tests. It was mentioned previously that the tangential length scales may have an important effect on the BPF tone level. The narrow tangential scales found in static tests but presumably absent in flight could account for the level fluctuations observed.

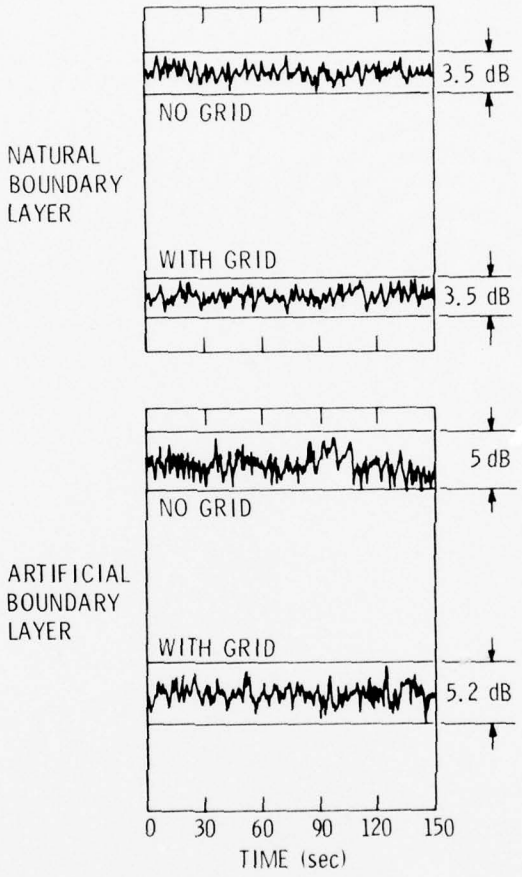

Figure 34. Blade Passing Frequency Tone Time Histories for Natural and Artificial Boundary Layers With and Without Grid, ϕ = 0.75, 5440 rpm, Seventeen Bladed Rotor.

CHAPTER V

CORRELATION OF TURBULENCE PARAMETERS WITH NOISE DATA

Previous investigations, both theoretical and experimental, have indicated that the sound power varies as the square of the turbulence intensities and inversely as the square of the turbulent axial integral length scales for a rotor interacting with isotropic turbulence. In the present investigation, a different correlation has been found. The sound power still varies as the square of turbulence intensities but inversely as the ratio of turbulent axial integral scale to blade spacing. With the ten bladed rotor operating with the grid, the proper mean inflow velocities could not be achieved; hence, the results do not appear in the correlations. The correlating parameter is $\overline{q^2}U_{rel}^4(L_x/S)^{-1}$, where L_x is the axial integral scale of the turbulence and $\overline{q^2}$ is the turbulence intensity normal to the blade defined by:

$$\overline{q^2} = \overline{v^2}\cos^2\zeta + 2\overline{uv}\sin\zeta\cos\zeta + \overline{u^2}\sin^2\zeta \quad , \tag{5.1}$$

where ζ is the stagger angle of the blade. The second term on the right hand side of Equation (5.1) is small and was neglected. The far-field sound pressure level (SPL) at BPF is correlated in Figures 35 and 36 and follow the relation:

$$SPL = (SPL)_0 + 40 \log U_{rel} + 10 \log \overline{q^2} - 10 \log L_x + 10 \log S \quad , \tag{5.2}$$

where $(SPL)_0$ is a constant base level.

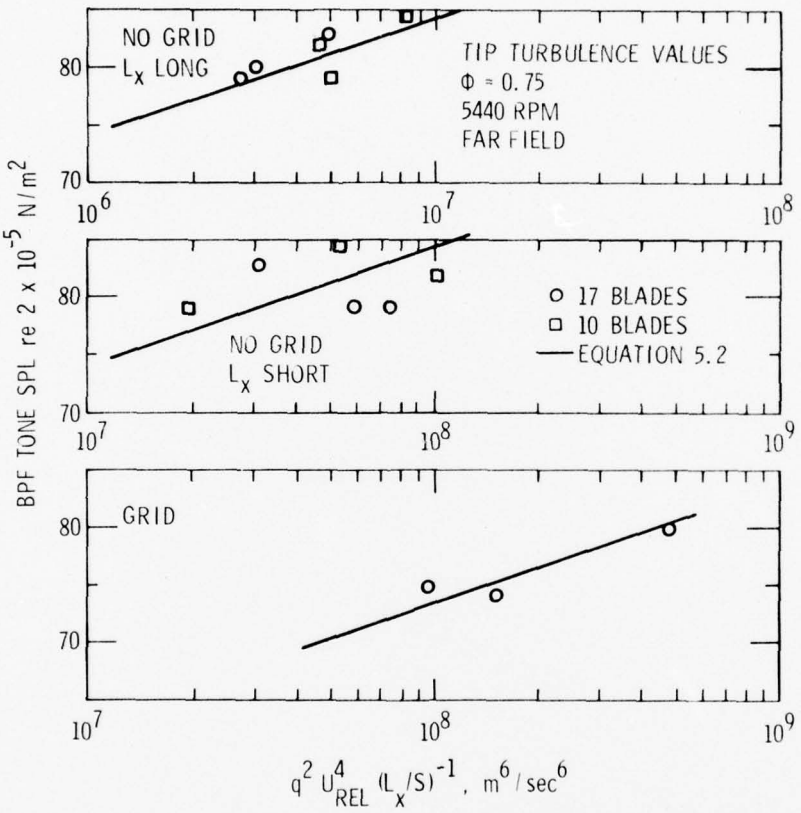

Figure 35. Correlation Between Blade Passing Frequency Tone Sound Pressure Level and Tip Turbulence Values.

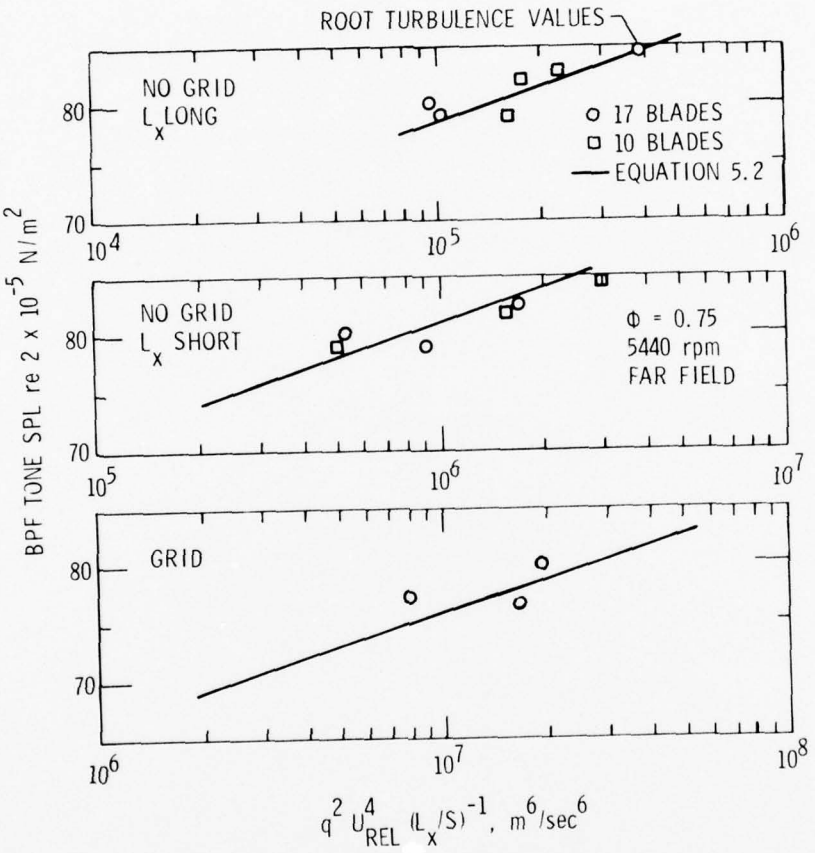

Figure 36. Correlation Between Blade Passing Frequency Tone Sound Pressure Level and Root Turbulence Parameters.

The values of the turbulence properties were taken from near the hub and near the tip of the rotor. The correlation with values at mid-radius was found to be poor (Figure 37). This appears to indicate that sound generation occurs primarily near the tip and root regions of the rotor which operate in the hub and annulus wall boundary layers.

The correlations in Figures 35 and 36 also indicate that the long axial length scale has a major influence on the BPF tones; however, the dependence of sound level on length scale is weak. The main effect of the long axial length scale is on the number and strength of higher harmonics of the BPF. This is clearly shown in Figures 21 and 22, where the sound spectra with and without the grid are compared. When the long scales were present (no grid), the second and third harmonic are present. When only the small scales were present (grid), these disappear. Hanson [18] reached a similar conclusion saying that the long length scales are responsible for the spectral distribution of sound energy; that is, they lead to narrow peaks in the noise spectra.

In Figures 38 and 39, the second BPF harmonic is plotted against the turbulence parameters with no grid installed. There were no points available for a correlation with the grid because of the length scale effect on BPF harmonic tones which results in a drastic reduction or elimination of the second and subsequent harmonics of the BPF tone.

Figures 40 and 41 show the results of the noise level at two kHz with the turbulence values at the tip and root of the rotor. There is little change in the quality of correlation for the short length scale as compared to Figures 34 and 35, but the correlation for the long

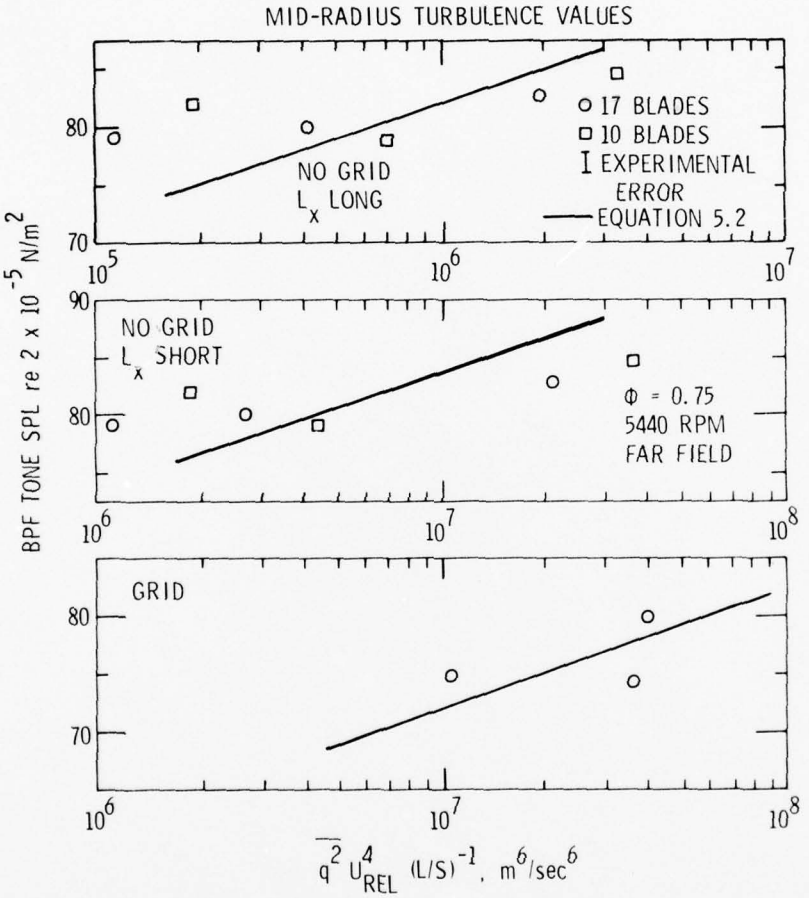

Figure 37. Correlation Between Blade Passing Frequency Tone Sound Pressure Level and Mid-Radius Turbulence Values.

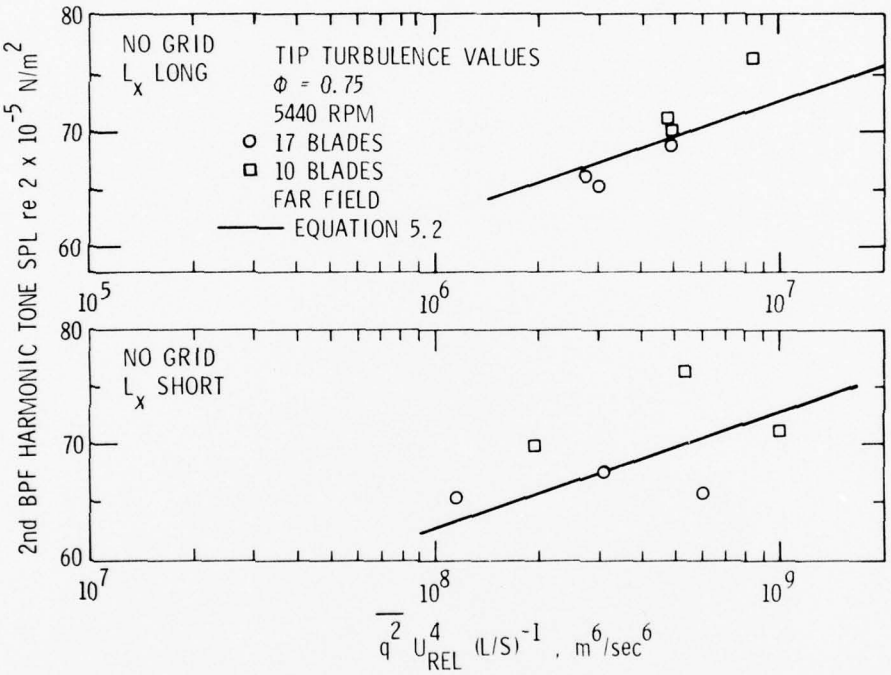

Figure 38. Correlation Between Blade Passing Frequency Second Harmonic Tone Sound Pressure Level and Tip Turbulence Values.

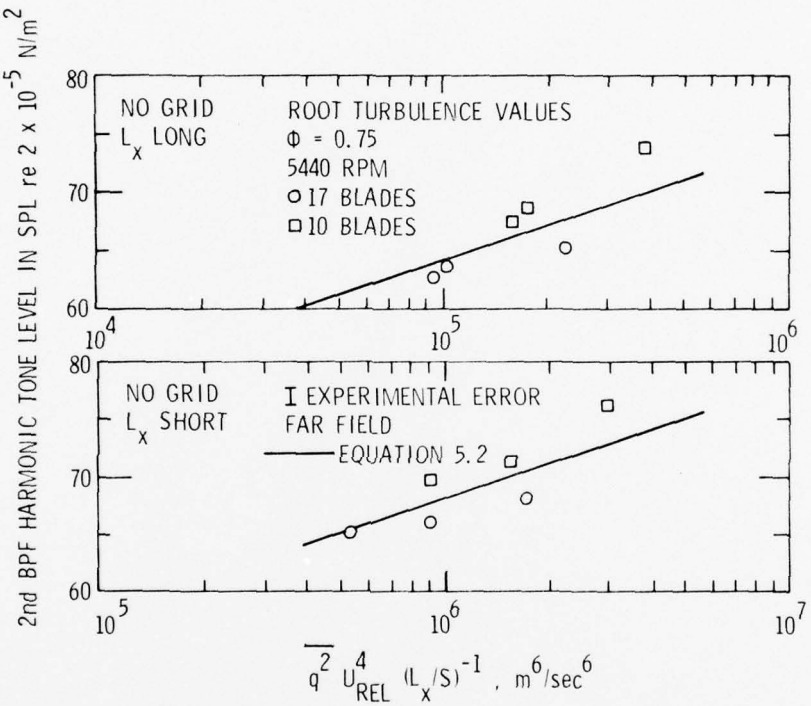

Figure 39. Correlation Between Second Blade Passing Frequency Harmonic Tone Sound Pressure Level and Root Turbulence Values.

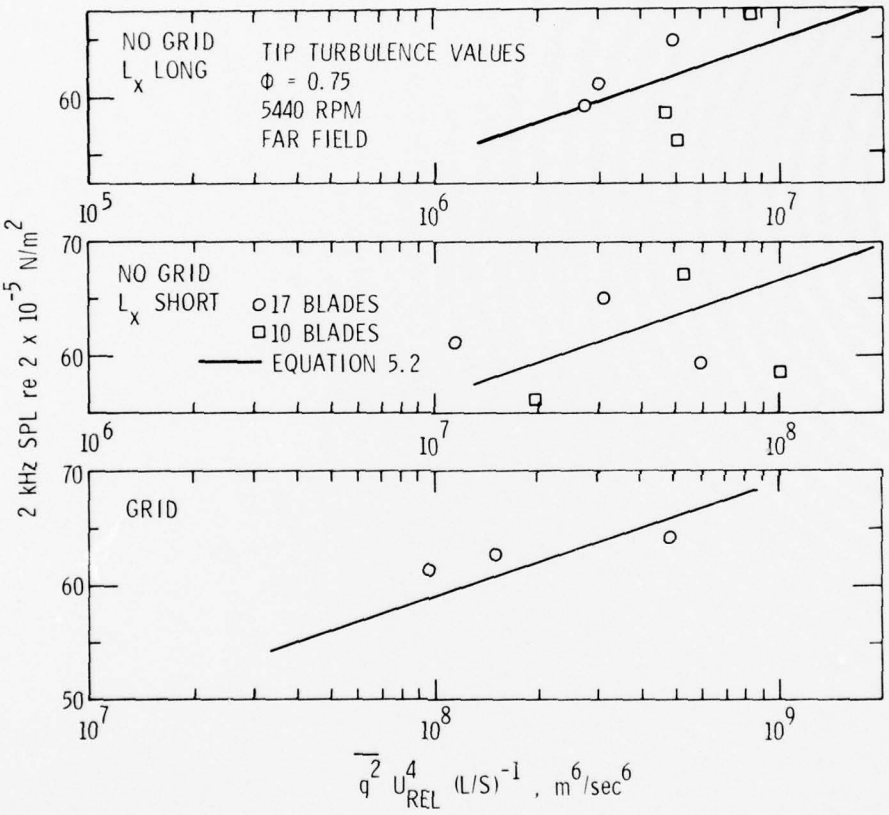

Figure 40. Correlation Between Sound Pressure Level at 2 kHz and Tip Turbulence Values.

AD-A040 946 PENNSYLVANIA STATE UNIV UNIVERSITY PARK APPLIED RESE--ETC F/G 20/1
NOISE DUE TO THE INTERACTION OF BOUNDARY LAYER TURBULENCE WITH --ETC(U)
OCT 76 N MOISEEV, B LAKSHMINARAYANA N00017-73-C-1418

UNCLASSIFIED TM-76-258 NL

2 OF 2
ADA040946

END

DATE
FILMED
7-77

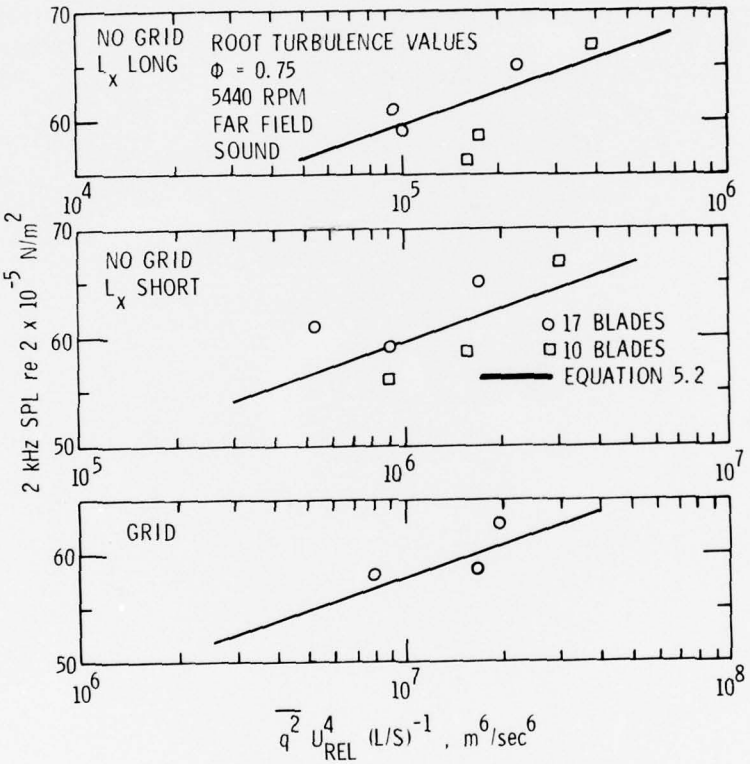

Figure 41. Correlation Between Sound Pressure Level at 2 kHz and Root Turbulence Values.

length scale has seriously deteriorated. This is further evidence that short length scales contribute primarily to broadband noise levels and long length scales are dominant for BPF harmonic tone levels. This trend continues at four kHz, see Figures 42 and 43.

No definite conclusions can be drawn with regard to the effect of the tangential scales on the sound spectrum. An interesting observation is that the tangential scales, L_θ, for the ABL were much less than the blade spacing, S. The BPF levels for the ABL were lower than either the NBL or FDBL, both of which had much higher L_θ/S ratios.

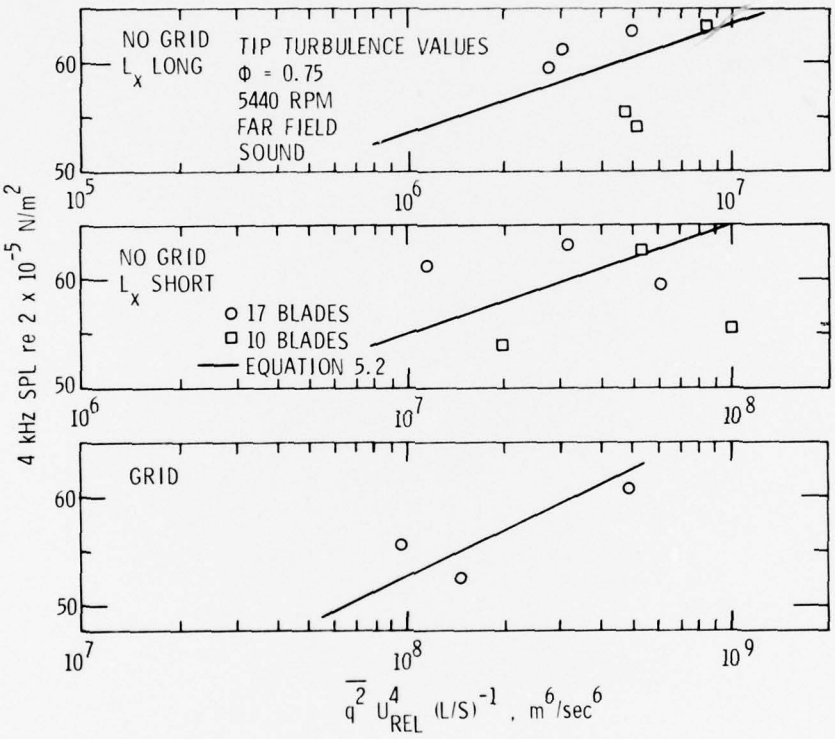

Figure 42. Correlation Between Sound Pressure Level at 4 kHz and Tip Turbulence Values.

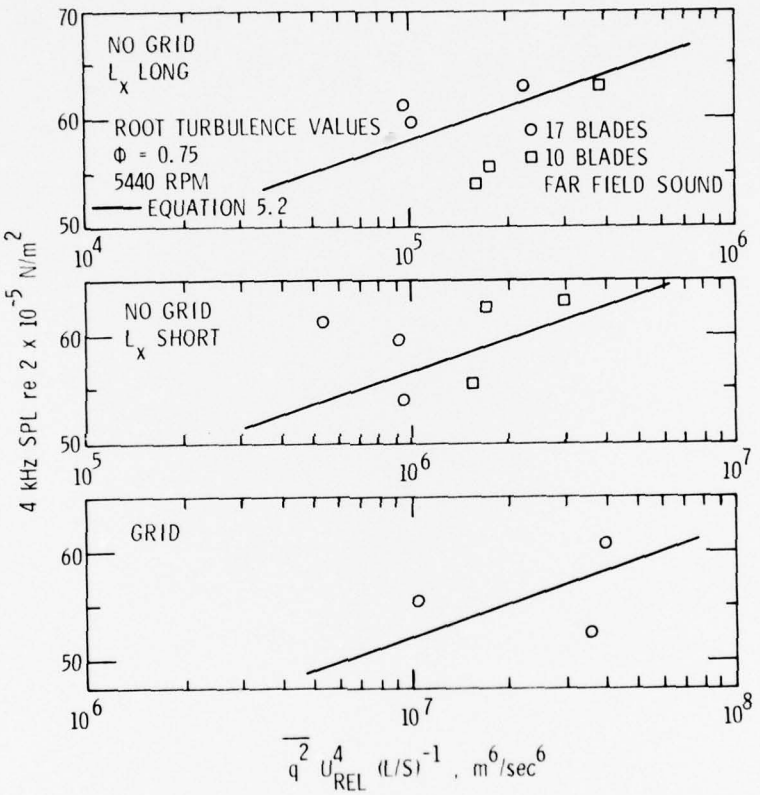

Figure 43. Correlation Between Sound Pressure Level at 4 kHz and Root Turbulence Values.

CHAPTER VI

CONCLUSIONS

The following conclusions can be drawn from this study whose objective is an understanding of the relationship between boundary layer inflow turbulence and the noise generated by its interaction with a blade row.

1. Two length scales of turbulence are found to exist simultaneously in the inflow of a static fan facility with no grid installed, long and short scales in the axial direction, narrow and wide in the tangential direction. The long axial scale disappears with a grid present.

2. Turbulence intensities are found to be maximum at the outer wall with appreciable magnitudes found even at mid-radius where the turbulence is primarily from the free stream.

3. The controlling factors in noise generation are the turbulence intensity and length scale. An empirical relation [Equation (5.2)] has been developed between these turbulence properties and radiated noise levels. The source of the turbulence does not seem to make any difference. Both boundary layer and atmospheric turbulence have the same effects. Atmospheric turbulence does, however, influence boundary layer turbulence.

4. The long axial length scales appear to be a strong factor in determining the number and strength of blade passing frequency harmonics. Short axial length scales contribute primarily to the general broadband

noise levels. These major differences between the effect of long and short length scales seem to account for the discrepancies between in-flight and static noise tests.

5. The primary sources of sound radiated from the rotor appear from the correlations, Section V, to be the root and tip regions for the particular hub-rotor configuration tested. Since these regions often operate in boundary layers, boundary layer turbulence can be an important source of radiated noise.

6. Mani's [4] prediction that with a decreasing ratio of axial integral length scale to blade spacing (for nearly isotropic turbulence), the general noise level will increase and the blade passing frequency peaks will broaden seems to be borne out by the comparison between seventeen- and ten-bladed rotor spectra with identical entry turbulence.

7. The measurements indicate that the noise level, particularly at the blade passing frequency, depends on the tangential scales, but no quantitative conclusions could be drawn.

8. Changes in the blade loading affect the number of blade passing frequency tones present in the sound spectrum. An increase in steady blade loading leads to an increase in harmonic tone levels.

BIBLIOGRAPHY

1. Ffowcs-Williams, J. E. and Hawkings, D. L., "Theory Relating to the Noise of Rotating Machinery," J. Sound and Vib. 10, 10-12, (1969).

2. Chandraschekhara, N., "Sound Radiation from Random Quadrupole Source Distributions in Axial Flow Fans," J. Sound and Vib. 19, 133, (1971).

3. Sevik, M., "Sound Radiation from a Subsonic Rotor Subjected to Turbulence," In Fluid Mechanics, Acoustics, and Design of Turbomachinery, Edited by B. Lakshminarayana, W. R. Britsch, W. S. Gearhart, Natl. Aeronaut. and Space Admin. Sp. Publ. 304, (Part II), 493, (1974).

4. Mani, R., "Noise Due to Interaction of Inlet Turbulence with Isolated Stators and Rotors," J. Sound and Vib. 17, 251-260, (1971).

5. Sears, W. R., "Some Aspects of Nonstationary Aerofoil Theory and Its Practical Application," J. Aeronaut. Sci. 8, 104-108, (1941).

6. Goldstein, M. E., "A Review of Recent Developments in Aircraft Engine Fan Noise Analysis," Shock and Vib. Digest 6, (1974).

7. Robbins, B. and Lakshminarayana, B., "Effect of Inlet Turbulence on Compressor Noise," J. Aircraft 2, 273-281, (1974).

8. Sofrin, T. G. and McCann, J. C., "Pratt and Whitney Experience in Compressor Noise Reduction," Acoust. Soc. Am. paper presented at Nov. 1-5, 1966 meeting, Los Angeles, CA.

9. Sharland, I. J., "Sources of Noise in Axial Flow Fans," J. Sound and Vib. 1, 302-322, (1964).

10. Curle, N., "The Influence of Solid Boundaries Upon Aerodynamic Sound," Proceedings of the Royal Society, 231A, 505-514, (1955).

11. Liepmann, H. W., "On the Application of Statistical Concepts of the Buffeting Problem," J. Aeronaut. Sci. 19, 793-800, (1952).

12. Morfey, C. L., "Broadband Sound Radiated from Subsonic Rotors," In Fluid Mechanics, Acoustics, and Design of Turbomachinery, edited by B. Lakshminarayana, W. R. Britsch, W. S. Gearhart, Natl. Aeronaut. and Space Admin. Sp. Publ. 304, (Part II), 461, (1974).

13. Mugridge, B. D. and Morfey, C. L., "Sources of Noise in Axial Flow Fans," J. Acoust. Soc. Am. 51, 1411-1426, (1972).

14. Thompson, D. E., "Propellor Time-Dependent Force Due to Nonuniform Flow," a Doctor of Philosophy thesis in Aerospace Engineering, The Pennsylvania State University, (1976).

15. Pickett, G. F., "Effects of Nonuniform Inflow on Fan Noise," Acoust. Soc. Am. paper presented at April 23-26, 1974 meeting, New York City, NY.

16. Mugridge, B. D., "Gust Loading on a Thin Airfoil," The Aeronaut. Quarterly 22, (Part III), 301-310, (1971).

17. Lowson, M. V., "Rotor Noise Radiation in Nonuniform Flow," Paper D2 Aerodynamic Noise Symposium, September 1970, Loughborough University of Technology, England.

18. Hanson, D. B., "A Study of Subsonic Fan Noise Caused by Atmosphere Turbulence," J. Acoust. Soc. Am. 56, 110-126, (1974).

19. Homicz, G. F. and George, A. R., "Broadband and Discrete Frequency Radiation from Subsonic Rotors," J. Sound and Vib. 36, 151-177, (1974).

20. Lowson, M. V., Whatmore, A. R., and Whitfield, C. E., "Source Mechanisms for Rotor Noise Radiation," Natl. Aeronaut. and Space Admin. Cont. Rep. 2077, (August 1973).

21 Lane, F., "Broadband Noise Generated by Turbulent Inflow to Rotor or Stator Blades in an Annular Duct," Natl. Aeronaut. and Space Admin. Cont. Rep. 2503, (March 1975).

22. Cumpsty, N. A. and Lowrie, B. W., "The Cause of Tone Generation by Aero Engines at High Subsonic Tip Speeds and the Effect of Forward Speed," Transactions of Am. Soc. Mech. Engrs. Series B, J. Eng. Power, 228-234, (1974)

23. Goldstein, M. E., Rosenbaum, B. M., and L. U. Albers, "Sound Radiation from a High Speed Axial Flow Fan Due to the Inlet Turbulence Quadrupole Interaction," Natl. Aeronaut. and Space Admin. Tech. Note D7667, (June 1974).

24. Robbins, B., "Turbulence Induced Noise in a Single Stage Axial Flow Fan," a Master of Science thesis in Aerospace Engineering, The Pennsylvania State University, (1974).

25. Von Frank, E. D., "Turbulence Characterisitics in the Mixing Region of a Unperturbed Round Jet," a Master of Science thesis in Aerospace Engineering, The Pennsylvania State University, (1970).

26. Horlock, J. H., Axial Flow Compressors, Butterworth, Inc., (1958).

27. Ingard, K. U. and Sighal, V. K., "Effect of Flow on the Acoustic Resonances of an Open-Ended Duct," J. Acoust. Soc. Am. 58, 788-793, (1975).

APPENDIX A

CALIBRATION OF SEMI-ANECHOIC CHAMBER

The semi-anechoic chamber was calibrated by driving a speaker with selected pure tones between 0.1 and 20 kHz and measuring the sound field in radial increments of 0.3 m. In one set of measurements, the speaker was 0.3 m off the center of the chamber; in another set, the source was 1.5 m off center. These measurements were conducted by E. Wong before subsequent modifications were made for the chamber's use with the aeroacoustic facility. The calibration carried out for the present experiment was made after the modifications outlined in Chapter III. The source speaker was set in the mouth of the inlet and the microphone traversed along the centerline of the rotor inlet in increments of 0.3 m. The bellmouth inlet and the inlet hole in the opposite wall were completely exposed during the test. The positions of the source and microphone for each test series and the results are shown in Figure 44.

The results show good agreement with the anechoic conditions of a 6 dB decrease in SPL per each doubling of distance from 0.1 to 20 kHz for both the normal configuration and the configuration of interest to this study.

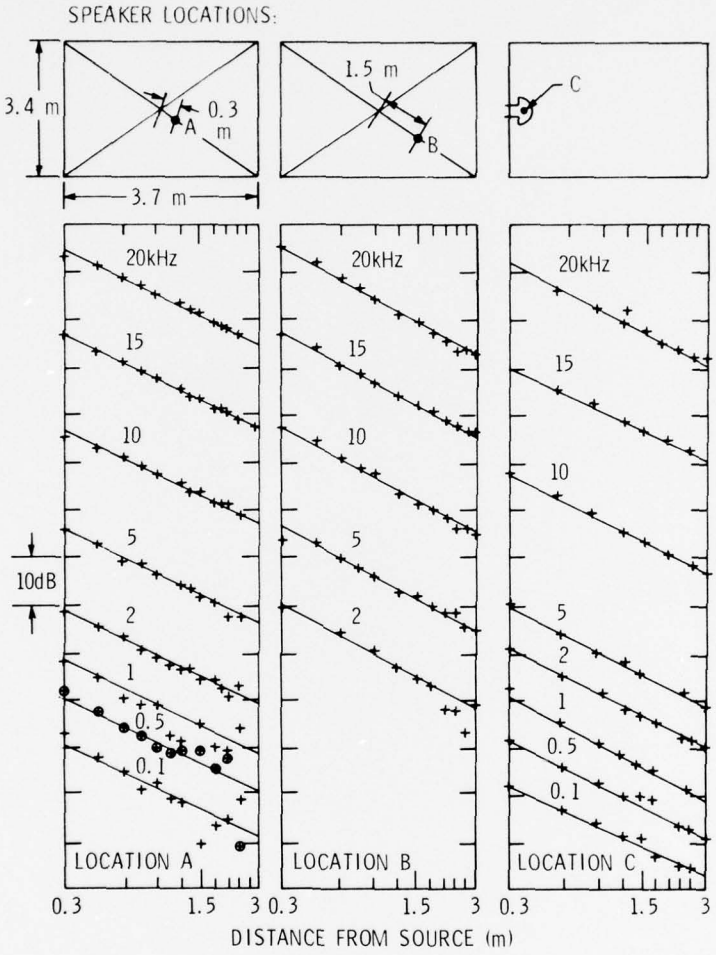

Figure 44. Inverse Square Law Test for Semi-Anechoic Room.

APPENDIX B

STEADY STATE CHARACTERISTICS OF TEST ROTOR

The steady state operating characteristics of the seventeen bladed test rotor were determined in terms of the flow, drag, lift, and static pressure and stage loading coefficients. These coefficients were calculated from measured stagnation and static pressures as well as the angle of the flow. The rotor operating conditions are listed in Table VI.

TABLE VI

ROTOR OPERATING CONDITIONS - STEADY STATE TEST

ϕ (flow coefficient)	Rotor RPM	Axial Velocity
0.629	6380	36.9 m/sec
0.750	5440	39.0 m/sec
0.871	5440	43.3 m/sec

Measurements of the stagnation pressures, static pressures, and exit flow angles were carried out with a YC 120 wedge probe from Universal Sensors at 15 radial positions two chords downstream of the rotor as shown in Figure 6. The pressures were measured with a pressure transducer, the output of which was measured with a DC integrating voltmeter. The flow angles were determined by using the transducer-voltmeter pair as a nulling circuit when the transducer was placed across the two static pressure tubes of the probe.

The static pressure was corrected for error using the formula:

$$\frac{P_S - P_m}{P_0 - P_m} = 0.1 \quad ,$$

where P_S is the actual static pressure, P_m is the measured static pressure, and P_0 is the stagnation pressure.

The various coefficients were calculated from the following formulas. The symbols and equations used are those of Horlock [26],

$$C_L = 2(S/c)\cos \beta_m \left[\tan \beta_1 - \tan \beta_2\right] \quad ,$$

$$C_D = (\psi_0 - \psi_E) \frac{S}{c} \left(\frac{U_T}{W_M}\right)^2 \cos \beta_m \quad ,$$

$$\psi_0 = \frac{P_{0_2} - P_{0_1}}{\frac{1}{2} \rho U_T^2} \quad , \quad \psi_E = 2 \left(\frac{U_\theta}{U_T}\right)\left(\frac{r}{r_T}\right) \quad ,$$

$$\psi_S = \frac{P_{S_2} - P_{S_1}}{\frac{1}{2} \rho U_T^2} \quad \text{and} \quad \phi = \frac{U_c}{U_T} \quad ,$$

where β_1, β_2, β_m are inlet, exit and mean flow angles, respectively; P_{0_2}, P_{0_1}, and P_{S_2}, P_{S_1} are the exit and inlet, stagnation and static pressures, respectively; U_θ is the absolute tangential velocity at the exit.

The inlet mean velocity profiles are shown in Figure 8. The long ducting is responsible for the boundary layer, the effect of which is visible in the exit axial mean velocity profiles in Figure 45.

Figures 46 and 47 show the stage loading and static pressure coefficients versus radial position. For the flow coefficient 0.871, the stage loading and static pressure coefficients are nearly the same

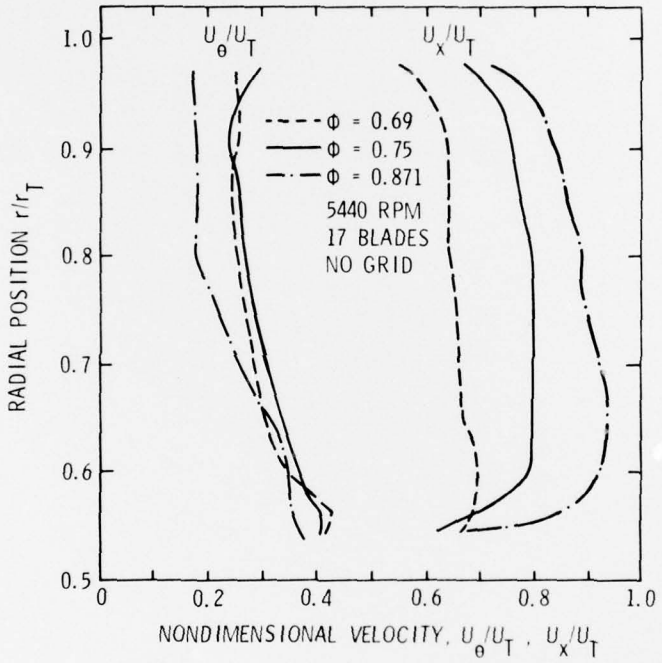

Figure 45. Exit Velocity Profiles.

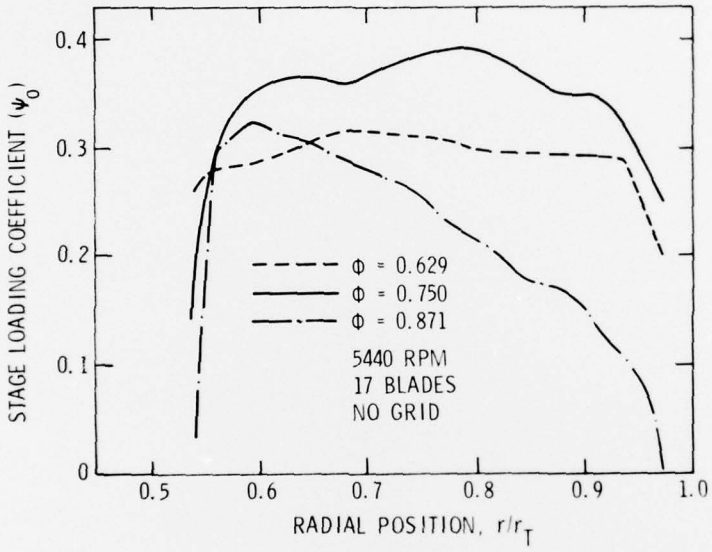

Figure 46. Stage Loading Coefficient vs. Radial Position.

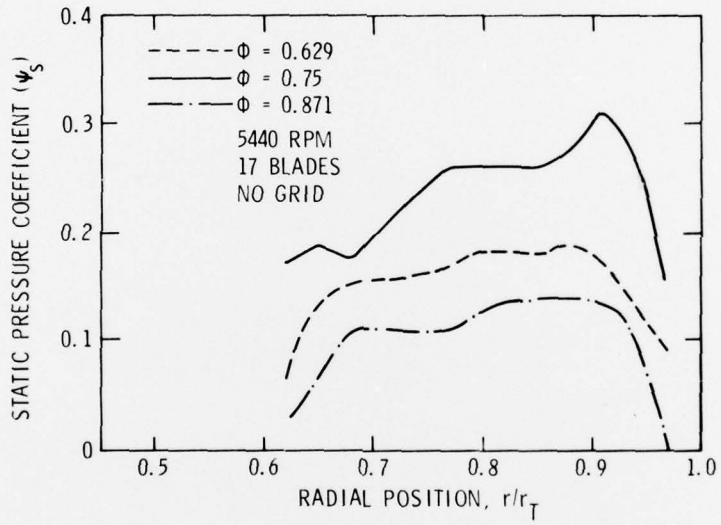

Figure 47. Static Pressure Coefficient vs. Radial Position.

in the tip region. This indicates a zero tangential velocity which, as seen in Figure 45, is not true. This contradiction implies an error for the coefficients in the tip region. This error is probably in the static pressure measurements and is attributed to the highly turbulent nature of the flow in this region of the boundary layer on the annulus wall. The measured values of C_L and C_D are shown in Figures 48 and 49, respectively.

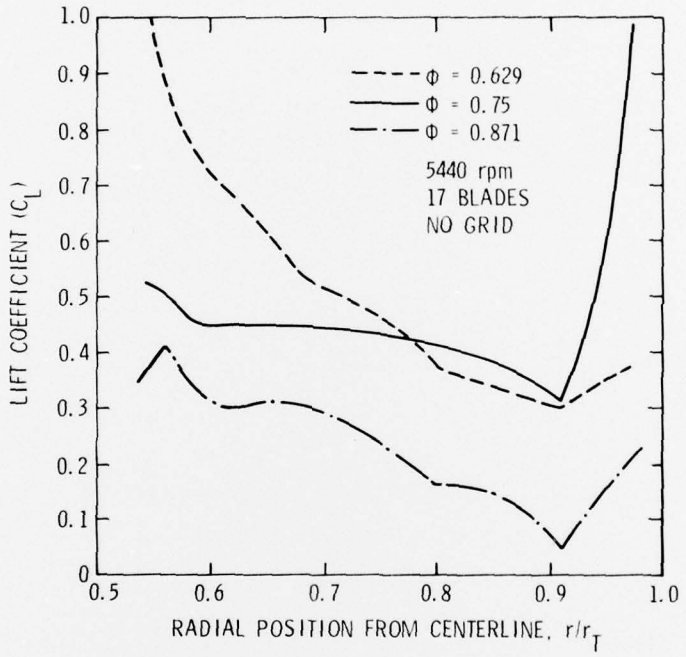

Figure 48. Lift Coefficient vs. Radial Position.

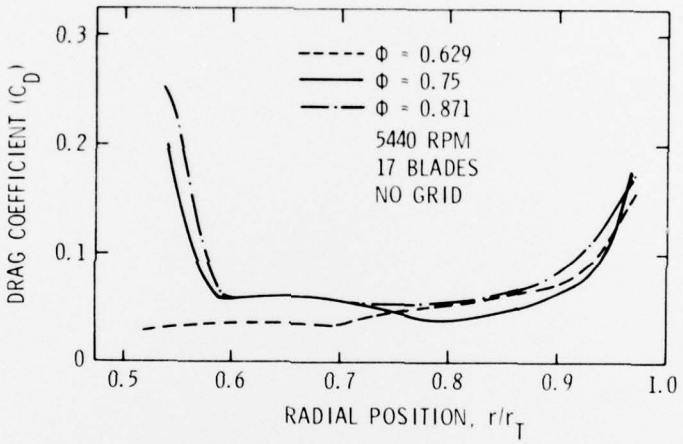

Figure 49. Drag Coefficient vs. Radial Position.

APPENDIX C

ATTEMPTS TO ACHIEVE FULLY DEVELOPED BOUNDARY LAYER FLOW

Several methods, shown in Figure 50, were discussed and tried before a fully developed boundary layer was achieved. The first attempt was an 0.53-cm thick o-ring placed before the transition point on the nose cone in order to trigger earlier transition to turbulent flow and to achieve faster boundary layer growth, see Figure 50(a). It led to a small increase in boundary layer and a steeper slope than the natural boundary layer as shown in Figure 51A but did not follow a power law development. A 0.318-cm thick o-ring placed downstream of the nose cone [see Figure 4(b)] led to some increase in the boundary layer thickness and a steeper slope that did follow a power law. It was used in the experiment and labeled the ABL. A series of 0.138-cm thick o-rings placed 0.76 cm apart on the hub had the same effect as one o-ring.

Two staggered lines of screws placed 2.54 cm apart on the nose cone, as shown in Figure 50(b), resulted in a very thick boundary layer. Its length scales were thought to be too different from a normal boundary layer so it was not used. It also produced excessive noise for the purposes of this study. The profile developed is shown in Figure 51A.

A coating of rough sandpaper for 25.4 cm in length on the hub was tried, see Figure 50(c). It led to a velocity profile as shown in Figure 51A. It had a much steeper slope than the NBL but had no increase in thickness.

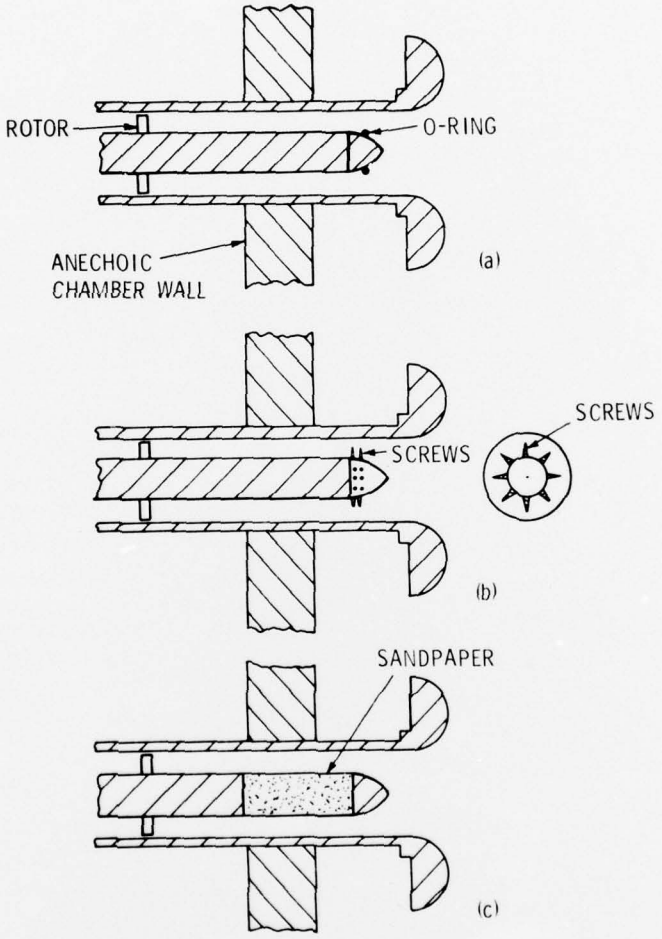

Figure 50. Cross-Section View of Boundary Layer Configurations: (a) O-Ring Transition Trip, (b) Screws, (c) Sandpaper Alone.

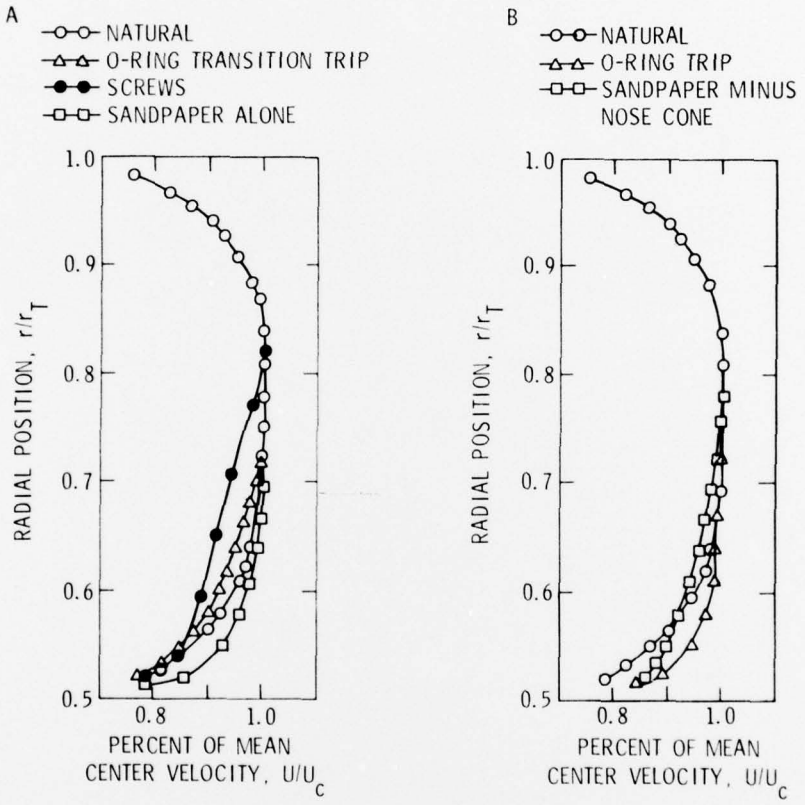

Figure 51. Inlet Velocity Profiles.

The final and successful attempt was to keep the sandpaper and remove the nose cone, as shown in Figure 4(c). It led to the FDBL whose very steep, thick velocity profile is shown in Figure 51B.

APPENDIX D

CALIBRATION OF THE ACOUSTIC RESPONSE OF THE INLET DUCT

Measurement of the acoustic response of the inlet duct was performed utilizing the reciprocity principle because the small size of the annulus prohibited the placing of an adequate source in the duct. Reciprocity is the principle by which the source and receiver in a sound field may exchange positions leaving the sound field unchanged. The measurements were taken with and without flow. It was concluded that the frequency shift of the duct modes, as observed by Ingard and Singhal [28] and others, would be reversed when employing the reciprocity principle in a flow field. Also, the low mach number of the flow and the short length of the duct means that any effect of the flow on the acoustic response would be negligible.

A 1/4-inch B & K microphone was positioned in the duct where the rotor normally was placed. A random noise signal was broadcast through a speaker placed in the anechoic chamber in the position the microphone occupied during the measurement of the rotor noise. The microphone response was displayed through a real time analyzer with a 30 Hz bandwidth and averaged over 1024 ensembles. The output was recorded on paper by an x-y plotter. The microphone response while in the duct was compared to the microphone response when both it and the speaker were in the chamber at the same distance of separation as when the microphone was in the duct. The ratio of the in-duct sound pressure to the in-chamber sound pressure was defined as the response of the duct.

This means that the sound pressure level, SPL, from the in-chamber configuration was substracted from the SPL of the in-duct configuration. This was performed for both the grid and no grid configurations for all three boundary layer set-ups as follows:

$$\text{Duct Response} = 20 \log \frac{P_2}{P_0} - 20 \log \frac{P_1}{P_0} = 20 \log \frac{P_2}{P_1} \quad ,$$

where

P_2 = sound pressure when microphone is in duct,

P_1 = sound pressure when microphone is in chamber

and P_0 = reference sound pressure 2×10^{-5} N/m^2.

The three configurations used to generate the three boundary layers are shown in Figure 4. The acoustic response was identical for all configurations. The grid also had no effect on sound propagation. Apparently, the nose cone tapers off so quickly that acoustically it is as if there was a blunt body in the duct as we have for the fully developed configuration. The acoustic response of the duct is shown in Figure 52 and is identical for all configurations. The peak at 4 kHz corresponds to a wavelength twice the size of the annulus and thus is the first mode of the duct. The peaks at 6.0 and 8.5 kHz correspond to higher modes which are not of interest in this investigation.

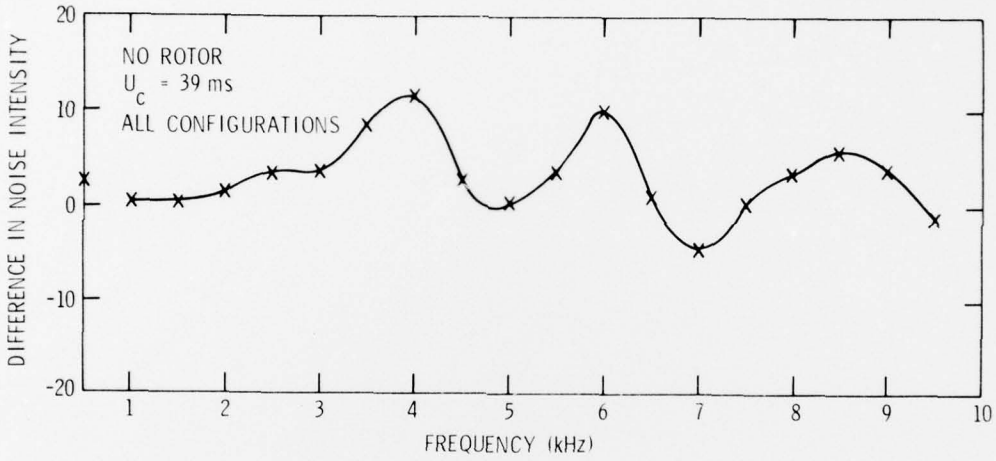

Figure 52. Acoustic Response of Duct.

DISTRIBUTION FOR UNCLASSIFIED TM 76-258 by Neil Moiseev, B. Lakshminarayana and D. E. Thompson

Commander (NSEA 09G32)
Naval Sea Systems Command
Department of the Navy
Washington, D. C. 20362
(Copies 1 and 2)

Commander (NSEA 0342)
Naval Sea Systems Command
Department of the Navy
Washington, D. C. 20362
(Copies 3 and 4)

Defense Documentation Center
5010 Duke Street
Cameron Station
Alexandria, VA 22314
(Copies 5 - 16)

Commander
Naval Sea Systems Command
Department of the Navy
Washington, D. C. 20362

Naval Sea Systems Command
Attn: T. E. Peirce
Code NSEA-0351
(Copy 17)

Naval Sea Systems Command
Attn: A. R. Paladino
Code NSEA-0372
(Copy 18)

Commanding Officer & Director
David W. Taylor Naval Ship R&D Center
Department of the Navy
Bethesda, MD 20084
Attn: S. F. Crump
Code 1505
(Copy 19)

David W. Taylor Naval Ship R&D Center
Attn: W. B. Morgan
Code 154
(Copy 20)

David W. Taylor Naval Ship R&D Center
Attn: R. Cumming
Code 1544
(Copy 21)

David W. Taylor Naval Ship R&D Center
Attn: J. McCarthy
Code 1552
(Copy 22)

David W. Taylor Naval Ship R&D Center
Attn: M. Sevik
Code 19
(Copy 23)

David W. Taylor Naval Ship R&D Center
Attn: W. Blake
Code 1942
(Copy 24)

Dr. R. C. Dean, Jr.
President, Creare, Inc.
Box 71
Hanover, NH 03755
(Copy 25)

Mr. C. Feiler
NASA Lewis Research Center
21000 Brookpark Road
Cleveland, OH 41135
(Copy 26)

Dr. W. Folay
United Aircraft Res. Lab.
Silver Lane
East Hartford, CT 06108
(Copy 27)

Dr. Don Hanson
Mail Stop 1A-3-6
Hamilton Standard
Windsor Locks, CT 06096
(Copy 28)

Mr. M. J. Hartmann
NASA Lewis Research Center
21000 Brookpark Road
Cleveland, OH 41135
(Copy 29)

Sir William Hawthorne
Head of Engr. Dept.
University of Cambridge
Trumpington Street
Cambridge, ENGLAND
(Copy 30)

(Distribution for TM 76-258 Cont'd)

Mr. M. Heidmann
MS-501-4
NASA Lewis Research Center
21000 Brookpark Road
Cleveland, OH 44135
(Copy 31)

Dr. J. H. Horlock
Vice-Chancellor
University of Salford
Salford, M5 4WT
ENGLAND
(Copy 32)

Dr. H. H. Hubbard
NASA Langley Research Center
Langley
Hampton, VA
(Copy 33)

Dr. J. L. Kerrebrock
Director, Gas Turbine Lab.
Mass. Institute of Tech.
Room 31-264
Cambridge 39, Mass.
(Copy 34)

Mr. J. D. Kester
Engineering Building
Pratt & Whitney Aircraft
East Hartford, CT 06108
(Copy 35)

Dr. C. L. Morfey
Institute of Sound & Vibration
The University of Southampton
ENGLAND
(Copy 36)

Dr. Brant Hodder
NASA Ames Res. Lab.
Ames, CA
(Copy 37)